VHH characterization.Recombinant VHHs: Production, characterization and affinity

Eric Chabrol, Johann Stojko, Alexandre Nicolas, Thomas Botzanowski, Benjamin Fould, Mathias Antoine, Sarah Cianférani, Gilles Ferry, Jean A. Boutin

VHH characterization.

Recombinant VHHs: production, characterization and affinity

Eric Chabrol[1&], Johann Stojko[1&], Alexandre Nicolas[1], Thomas Botzanowski[2], Benjamin Fould[1], Mathias Antoine[1], Sarah Cianférani[2], Gilles Ferry[1], Jean A. Boutin[1,3,*]

[1] PEX Biotechnologies, Chimie, Biologie, Institut de Recherches Servier, 125 chemin de Ronde, 78290 Croissy-sur-Seine, France

[2] Laboratoire de Spectrométrie de Masse BioOrganique, Université de Strasbourg, CNRS, IPHC, UMR 7178, 67000 Strasbourg, France

[3] Institut de Recherches Internationales Servier, 50 rue Carnot, 92284 Suresnes Cedex, France

[&] These two authors contributed equally to the work

***** To whom correspondence should be addressed: Dr. JA Boutin, Institut de Recherches Internationales Servier, 50 rue Carnot, 92284 Suresnes Cedex, France. Email : jean.boutin@servier.com; phone : +33155724400

Running title: VHH expression and characterization

Total number of manuscript pages: 41

Tables: 8

Figures: 10

Highlights:

- VHH are small antibody-like proteins. They are entering the therapeutic arsenal.
- VHH purity, homogeneity, structure and affinity towards their targets are described.
- An analytical workflow to qualify those proteins is presented to validate the molecules.

Abstract: Among the biological approaches to therapeutics, are the cells, such as CAR-T cells engineered or not, the antibodies armed or not, and the smaller protein scaffolds that can be modified to render them specific of other proteins, *à la façon* of antibodies. For several years, we explored ways to substitute antibodies by nanobodies (also known as VHHs), the smallest recognizing part of camelids' heavy-chain antibodies: production of those small proteins in host microorganisms, minute analyses, characterization, and qualification of their affinity towards designed targets. Here, we present three standard VHHs described in the literature: anti-albumin, anti-EGF receptor and anti-HER2, a typical cancer cell surface - associated protein. Because they differ slightly in global structure, they are good models to assess our body of analytical methodologies. The VHHs were expressed in several bacteria strains in order to identify and overcome the bottlenecks to obtain homogeneous preparations of this protein. A large panel of biophysical tools, ranging from spectroscopy to mass spectrometry, was here combined to assess VHH structural features and the impact of the disulfide bond. The routes are now ready to move to more complex VHHs raised against specific targets in numerous areas including oncology.

Keywords: VHH, expression, characterization, structure, affinity, CD, differential scanning fluorimetry, mass spectrometry, ion-mobility, hydrogen/deuterium exchange, surface plasmon resonnance.

1. INTRODUCTION:

Antibody therapy has taken a new boost these last years, due to the generalization of recombinant protein production techniques, on one hand and to the use of armed antibodies (Ab) on the other [1,2]. Indeed, several huge successes were recorded in many therapeutic areas, including, but not limited to cancer [3], diabetes [4], poisoning [5], immune-inflammation [6], and infectious diseases [7].

Anti-cancer therapy has been one of the main sources of progress [8] in this area, especially by pioneering and using in clinic armed antibodies also known as antibody-drug conjugates (ADCs) [9]. Basically, this consists to load a cytotoxic compound on an antibody and use it as a cargo to selectively deliver the conjugated drug on its target: a cell expressing the protein against which it has been raised [10]. The goal is to deliver the payload to the cancer cells with a higher efficiency thanks to the selectivity of the antibody, in order to potentializing its efficacy while diminishing its off-target effects (see Thomas *et al* for review [11]). Although this has been a breakthrough in the anticancer armada, with numerous successful examples [12–15], this approach essentially suffers from practical obstacles: the recombinant synthesis of those antibodies is not only tricky but also quite expensive, even if the amount of this product injected to patients remains, in some cases but not all, remarkably small due to the high affinity of the antibody for its target [16]. Furthermore, once purified to apparent homogeneity, antibodies usually include an intrinsic micro-heterogeneity, essentially due to many possible minute modifications - including glycosylations [17,18] - of some amino acids in the Ab heavy chain (see for example Husson *et al* [19]). This heterogeneity can be further increased by chemical modifications induced upon conjugation of the antibody with a cytotoxic compound, leading to new chemical species containing the monoclonal antibody (150 kDa) as well as a defined number of molecules of the cytotoxic compound [16]. Despite those difficulties and the obvious benefit brought to the patients, many progresses should and will be done in the future.

Alternative approaches are scrutinized, and particularly those concerning smaller protein molecules such as ankyrin (see review by Skerra [20]). The original idea was to take advantage of the particular single heavy chain antibody from camelids and sharks [21]. Indeed, the smallest intact antigen-binding part of those huge proteins is the variable domain of the heavy chain [22,23]. Those protein parts were called nanobodies or VHHs. Their sequences retain the antibody specificity for the targets they were raised against. Therefore, a smaller and less complex protein recognizing a given target could be used as a substitute to monoclonal antibodies. VHHs have been reported against many proteins that are supposedly preferentially expressed in cancer cells, such as PD-1 [24], EGFR [25], HER2 [26], HLA-DR [27],

GFRA1 [28], HSA [29] and many others. Needless to stress that the beauty of the approach relies on the specific nature of the protein expressed at the surface of the targeted cells (cancerous or others) and recognized by the VHHs. An anti-HER2 VHHs have been shown to be valuable tools for breast cancer cells detection [30–32]. Aside from oncology, those tools could also be used in many different application areas, including diagnosis [33].

To date, however, there is a clear deficit in peptide (and protein) characterization, particularly regarding their homogeneity [34]. Despite clear warnings in excellent reviews on the subject [35,36], as well as rapid progress in analytical methodologies, it still felt that many more characterization approaches should be systematically developed, in particular concerning therapeutic biologics [37] (as opposed to research biologics). Indeed, whenever a polypeptide is produced, whether from recombinant or synthetic approaches, it is too often assumed, on the unique basis of a SDS-PAGE electrophoresis and a liquid chromatography coupled to mass spectrometry analysis (LC-MS) that the peptide is pure and homogeneous, while the expected biological activity is at the *rendezvous*. A recent discussion on this subject has been put forward for synthetic peptide [34], while examples have been reported for recombinant proteins [19]. In fact, it is far from clear that such a limited characterization guarantees the homogeneity of the preparation, leading to a false interpretation about the amount of such polypeptide active in a given preparation. Led by this idea, we wanted to thoroughly describe the characteristics of VHHs, as they turned out to be promising alternatives to bigger biologics on the threshold of therapeutic use. While VHHs have been so far produced against many different targets, and very well characterized in terms of antigen recognition, their structure and overall biophysical characteristics yet remain scarcely documented.

In the present paper, we aimed at benchmarking the production and characterization workflows of VHH, using an anti-HER2 VHH as a model. This exploratory study, combining solution-based as well as gas-phase cutting edge approaches, enabled to broaden our functional and structural knowledge of this emerging class of proteins and laid the ground for future investigations. As we entered this new era during which small biologics, and particularly VHHs will take over as first intention drugs against cancers (see discussions on the various advantages of these solutions [38,39]), it will be crucial that the biochemical and analytical methods for a complete characterization of those entities become available with published backgrounds to help promoting and developing the rise of such molecules in the therapeutic arsenal.

2. Materials and methods

2.1 Cloning, expression and purification. Coding DNA fragments of the various VHHs have been *E.coli* codon optimized, synthetized and cloned into high copy expression vectors with a poly-His-tag at the C-terminal end of each protein. We used two different vectors, pET-15b and pET-20b, respectively for a cytoplasmic and periplasmic expression of the anti-HER2 VHH and only pET-15b for a cytoplasmic expression of both anti-HSA and anti-EGFR1 VHHs. The genetic constructs were transformed into two different *E.coli* strains for the anti-HER2 VHH: *Shuffle T7 express* and *BL21(DE3)* for the cytoplasmic and periplasmic expression respectively and only *Shuffle T7 express* strain for both anti-HSA and anti-EGFR1 VHHs. Bacteria were cultured in a LB medium with ampicillin (100 µg/mL final concentration) and the expression was induced with 0.1 mM IPTG when the OD at 600 nm reached 0.6. The temperature was decreased from 37°C to 22°C during expression that was carried on overnight. Cells were harvested by centrifugation (5000 g, 20 min, 4°C) and lysed by lysozyme membrane digestion (1 mg/mL) into a 20 mM Tris-HCl pH 8, 300 mM NaCl buffer supplemented with 10 µg/mL DNAse1 and protease inhibitor cocktail during 30 min at room temperature. Cell fragments were harvested by ultracentrifugation (100000 x g, 30 min, 4°C). The supernatant containing the his-tagged VHHs was then subjected to a three-steps purification. The supernatant was first injected onto an equilibrated Ni-NTA agarose resin (Qiagen) with a 20 mM Tris-HCl pH 8, 300 mM NaCl, 10 mM imidazole buffer. The column was washed with 20 mM imidazole and the proteins were eluted with 250 mM imidazole. The second purification step was performed by cation exchange chromatography (IEX, SourceS, GE healthcare) after dialysis of the sample against a buffer composed of 50 mM Tris-HCl pH 7.5, 50 mM NaCl. The sample was injected onto the cation exchange column previously equilibrated with the dialysis buffer. Elution was then achieved with a linear gradient of 1 M NaCl in 50 mM Tris-HCl pH 7.5. The eluted proteins were then concentrated on a 3 kDa MWCO Amicon device (Millipore). The concentrated sample was finally purified by sized exclusion chromatography (SEC) using a HiLoad 26/600 Superdex 200 column (GE Healthcare) equilibrated with a 50 mM Tris-HCl pH 7.5, 150 mM NaCl buffer.

2.2 Inclusion bodies (IB) expression and refolding of anti-HER2 VHH. The *BL21(DE3) E.coli* strain transformed with the pET15b vector containing the anti-HER2 VHH DNA was used to express the VHH in IB. Bacteria were cultured in a MagicMedia™ *E. coli* Expression Medium (ThermoFisher Scientific, Villebon, France) with ampicillin (final concentration at 100 µg/mL). The culture was performed overnight at 37°C following the supplier recommendation. Bacteria were then harvested by centrifugation (5000 x g, 20 min, 4°C) and lysed as previously described. After an ultracentrifugation step (100 000 x g, 20 min, 4°C), the supernatant was removed and stored for further use. The pellet was washed once with 30 mL/L of culture in a buffer composed of 20 mM Tris-HCl pH 8, 150 mM NaCl, 1 M Urea and 1%

Triton X-100 and resuspended using a 45 mL Potter-Elvehjem homogeneizer (Sigma). This preparation was then pelleted by ultracentrifugation (100000 x g, 30 min) at 4°C. Again, the supernatant was removed and stored. The resulting pellet was washed a second time using the same method but with a 20 mM Tris-HCl pH 8, 150 mM NaCl buffer. The wash solution was removed and stored, while the pellet was finally solubilized in 30 mL of 20 mM Tris-HCl pH 8, 6 M guanidium (Gdn) buffer using a Potter-Elvehjem homogeneizer. After an ultimate ultracentrifugation (100 000 x g, 30 min, 4 °C), all supernatant and wash fractions collected during the process and containing the denatured VHHs were mixed together in order to proceed to the refolding step. Therefore, the resulting sample was supplemented with 3 mM of reduced glutathione and 0.3 mM of oxidized glutathione then incubated at 4°C at a final concentration of 1 mg protein/mL for 48 h. The refolded proteins were then dialysed overnight at 4 °C against 100 volumes of a buffer containing 50 mM TAPS pH 8, 50 mM NaCl, 0.6 M Gdn and 0.8 M L-Arginine. The dialysis process was repeated using a 20 mM Tris-HCl pH 8 and 150 mM NaCl buffer until a one million final dialysis factor was reached. Purification was first performed by affinity chromatography as previously described and then by hydrophobic chromatography (HIC) to separate the oxidized from the reduced forms of the anti-HER2 VHH using a 5 mL butyl High Performance column (GE Healthcare) for 10 mg of injected proteins. Briefly, the refolded and dialyzed sample were diluted in a buffer comprising 100 mM phosphate pH 7.4 and 1.5 M ammonium sulphate, and injected on the column connected to an Akta FPLC instrument. The proteins were eluted using a gradient of the equilibrium buffer (100 mM NaH_2PO_4 pH 7.4). The fractions of interest were finally concentrated and dialysed in a 20 mM Tris-HCl pH 8, 150 mM NaCl buffer, before being used for further characterizations.

*2.3 Electrophoresis***.** SDS-Page experiments were performed using a 4-12 % Nu-Page® gel in MES buffer (Invitrogen, ThermoFisher) with a migration time of 90 minutes and a constant voltage of 120 V. The non-reduced samples (NR) were diluted in a LDS® buffer (Invitrogen) supplemented with 30 mM iodoacetamine and heated 2 min at 55°C. The reduced samples (R) diluted in a LDS® buffer supplemented with 50 mM DTT (Thermo Scientific Pierce) were boiled 5 min at 95°C. For each sample, about 2 µg of proteins were loaded onto the gels. The molecular weight reference was a SeeBlue Plus 2 Prestained Standard® (Invitrogen) and the Coomassie blue was a Quick Coomassie Stain® from Generon (Slough, UK). Images were captured with a Gel Doc™ EZ Gel.

2.4 Analytical light scattering. Analytical light scattering (ALS) analyses were performed using a 1260 Infinity HPLC (Agilent) coupled to a light scattering detector Dawn8+ HELEOS II® and a refractive index detector Optilab T-rex™ (Wyatt Technology, Santa Barbara, CA). The size exclusion column was a BioSec3, 3 µm, 100 Å, 4.6 x 300 mm (Agilent). The buffer used for the column equilibration and the sample dilution was composed of 50 mM Tris-HCl pH 7.5, 150 mM NaCl. All samples were diluted in the

running buffer to contain 20 µg of proteins for an injection of 30 µL with a flow rate of 0.2 mL/min. The data were collected and analyzed using the Astra® 6.1 software.

2.5 Circular dichroism (CD). Circular dichroism experiments were performed using a JASCO J-815 CD spectrometer coupled to a JASCO MCB-100 mini-circulation bath and a JASCO MPTC-490S/15 6-position Peltier Type Turret Cell Changer. The cuvettes used were Starna Scientific type 21/Q/1 quartz spectrophotometer cells with a path length of 1 mm. CD, high tension voltage (HT) and absorbance signals were collected from 190 to 260 nm with standard sensitivity and data pitch of 0.1 nm, a DIT of 1 sec, a bandwidth of 1 nm, a scanning speed of 50 nm/min, a temperature gradient of 0.5°C/min, a temperature interval of 5°C. Data were accumulated 5 times for each sample which was dialyzed against a 100 mM NaH_2PO_4 pH 7.5 buffer with a final concentration of 0.5 mg/mL. The formula used to calculate the ellipticity was the following: (33 x (A x 100) / (l x Protein concentration / MW x (number of residues – 1)) where A, l and MW correspond to the absorbance, the measure cell length and the molecular weight of the protein, respectively. The CD data were recorded at 25°C for each VHH and analysed using BeStSel, an online software enabling to calculate the proportion of secondary structures [44,43].

2.6 Differential scanning fluorimetry and light scattering. Differential scanning fluorimetry and light scattering experiments were performed on an OPTIM 2® instrument (AVACTA Analytical, Wetherby , UK). Briefly, intrinsic fluorescence and CD signals from each VHH sample were measured through a temperature ramp ranging from 25 °C to 90°C with an interval of 0.5°C/min and a starting incubation time of 120 s and the data collected was treated with the AVACTA Analysis software. Each experiment was performed in triplicate at a concentration of 2 mg/mL in a 50 mM Tris-HCl pH 7.5, 150 mM NaCl buffer. Data were finally processed using the AVACTA Analysis software v2.0.

2.7 Surface plasmon resonance. All experiments were performed on a Biacore T200 (GE Healthcare, Uppsala, Sweden) using a functionalized CM5 chip and the corresponding reagents from Biacore. Four flow-cells were activated by 50 µL of an EDC/NHS mixture. Flow-cell one was blocked with 50 µL of ethanolamine and used as a control surface. Flow-cell two three and four were functionalised up to a level of about 1000 resonance units (RU) with a 20 µg/mL solution of a recombinant human ErbB2 antigen (Sino Biological, Wayne, PA, USA, ref: 10004-H08H), a recombinant human EGFR1 antigen (Sino biological, ref: 10001-H08H) or a human serum albumin antigen (Sigma) in sodium acetate pH 5.0 buffer respectively. The immobilization procedure was performed in a PBS buffer (Biacore) supplemented with 0.005 % of P20 surfactant. Increasing amounts of each VHH were injected at a 50 µL/min flow rate in triplicate. The running buffer comprised 50 mM Tris-HCl pH 7.5, 150 mM NaCl supplemented with 0.005% P20 surfactant. Each protein was diluted twice into the running buffer with concentrations ranging

from 0.122 to 125 nM for anti-HER2 VHH, and from 0.195 to 100 nM for anti-EGFR1 VHH and anti-HSA VHH, respectively. The chips were regenerated with two cycles of 10-sec injections of 3 M $MgCl_2$ separated by a 900-sec delay. The association phase and dissociation phase were run during 4 or 6 min and 15 min respectively. Sensorgrams were fitted with Langmuir equation using the BIAeval software.

2.8 Liquid chromatography-mass spectrometry characterization of VHHs. UHPLC-MS analyses of VHH samples were performed on an Acquity UPLC H-Class Bio system (Waters, Manchester, UK) coupled to a Q-TOF mass spectrometer (Xevo G2-XS, Waters, Manchester, UK). A volume corresponding to 140 pmol of each sample was injected onto a reverse phase liquid chromatography column (BEH C4, 150 x 2.1 mm, 300Å, 1.7 µm, Waters). Sample elution was carried-out at 40°C from mobile phases A (water, 0.1% FA) and B (acetonitrile, 0.1% FA) using a flow rate of 0.2 mL/min and a 38-min gradient applied as follows: 0% B during 1 min, 0 to 10% B in 0.1 min, 10% to 40% B in 29.9 min, 40% to 90% in 2 min, 90% to 0% B in 0.1 min, 0% B during 4.9 min. Signal acquisition was realized by both UV absorbance measurement at 280 nm and mass spectrometry. The instrument was set in the positive ion mode with a capillary voltage, a desolvation gas flow, a sampling cone voltage and a source temperature of 1.5 kV, 800 L/h, 80 V and 120 °C respectively. MS spectra were recorded in the mass range of 500–4000 m/z with a scan time of 1 s. Calibration was performed using the singly charged ions produced by sodium iodide clusters diluted to 2 g/L in a 1:1 (v/v) water:isopropanol solution, and an online mass correction with Leu-enkephalin peptide as the lock mass. Data processing was carried out on Mass Lynx V4.1 (Waters, Manchester, UK). Relative quantification of chromatographically resolved species was performed by integrating their corresponding UV peak area.

2.9 Denaturing and native mass spectrometry. Anti-HER2 VHH samples were first buffer exchanged against a 100 mM ammonium acetate (NH4Ac) solution at pH 7.5 using gel filtration (Zeba 0.5 ml, Thermo Scientific, Rockford, IL, USA). Protein concentration was determined spectrophotometrically. NanoESI-MS characterization of these samples was next generated on a hybrid Q-TOF mass spectrometer with an ion mobility cell (Synapt G2-S HDMS, Waters, Manchester, UK) equipped with an automated chip-based nanoESI source (Triversa Nanomate, Advion Biosciences, Ithaca, NY, USA) operating in the positive ion mode. External calibrations were generated from the multiple charged ions produced by a 2µM horse heart myoglobin solution diluted in a 1:1 (v/v) water:acetonitrile mixture acidified with 1% (v/v) formic acid, and caesium iodide clusters diluted to 2 g/L in a 1:1 (v/v) water:isopropanol solution. Intact masses of anti-HER2 VHHs were first determined in denaturing conditions by diluting the samples to 2µM in a 1:1(v/v) water/acetonitrile mixture acidified with 1% (v/v) formic acid. Native protein analysis in non-denaturing conditions was then performed by diluting samples to 5µM in 100 mM NH4Ac buffer at pH 7.5. Fine-tuning of instrumental parameters was notably applied to preserve native 3D

structures in the gas phase and ensure efficient ion desolvation and transmission. Particularly, the Synapt G2-S source back-pressure was equal to 4.5 mbar while the acceleration voltages applied on the sample cone as well as in the trap cell were set to 40 and 4 V, respectively. Data processing was finally carried out on MassLynx V4.1 (Waters, Manchester, UK).

2.10 Native HDX-MS. The protocol was similar to those previously described in native MS, except that D_2O incubations were triggered by a 20-fold dilution of NH_4Ac buffer-exchanged anti-HER2 VHH samples in the same but deuterated 100 mM NH_4Ac buffer at pD 7.5 before infusion (95% final deuterium content). Mixtures were prepared in triplicates and analyzed by native MS in rigorously identical conditions, across an incubation time window ranging from 1 minute to 1 hour. Instrumental conditions were slightly refined (sampling cone and trap acceleration voltages respectively raised to 150 and 20V) to achieve a complete ion desolvation required for accurate deuterium uptake measurements.

2.11 Ion-mobility mass spectrometry (IM-MS). IM-MS experiments were performed on the abovementioned mass spectrometer. Fine-tuning of the instrument enabled to achieve a good trade-off between native ion preservation, desolvation, separation and TWIMS resolution. Low accelerating voltages were used, especially before IM separation, to guide the ions through the mobility cell to the TOF analyzer without ion activation. Specifically, the Synapt G2-S source back pressure and sampling cone voltage were equal to 5.1 mbar and 20 V, respectively. The argon flow rate and the collision energy inside the ion trap cell were fixed to 2.5 mL/min and 5V, respectively. Prior to IM separation, ions were thermalized in the helium cell (140 mL/min). Ion separation was performed in the pressurized ion mobility cell using a constant N_2 flow rate of 30 mL/min. The IM wave height and velocity were respectively set to 35 V and 1334 m/s. Transfer collision energy was fixed to 2 V to extract the ions from the IM cell to the TOF analyzer. Arrival time distributions (ATDs) and collisional cross sections ($^{TW}CCS_{N2\rightarrow He}$) of oxidized and reduced 8^+ ions were extracted and determined in their native (Trap CE = 5 V) and gas-phase activated conformations (Trap CE = 15 and 60 V) using an appropriate IM calibration (cytochrome-c and β-lactoglobulin native ions used as external calibrants [40,41]). Drift time (t_D) and $^{TW}CCS_{N2\rightarrow He}$ values for each conformer were finally expressed as an average measured in triplicate on the 8^+ charge state.

2.12 Collision induced unfolding (CIU) experiments. ATDs were recorded in triplicate by gradually increasing the trap collision energy in the traveling-wave-based ion trap before the IM cell. All the ions were accelerated into the ion trap without any previous selection. However, only ion mobility data corresponding to the 8+ charge state of studied samples were compiled to create the averaged CIU fingerprints. The trap collision energy was ramped from 0 to 120 V using an energy interval of 5 V. This voltage interval corresponds to the best trade-off between CIU fingerprint resolution and acquisition time. 2D CIU fingerprint plots were analysed using the open source CIUSuite software, especially the

CIUSuite_stats and CIUSuite_compare modules [42]. Briefly, these modules allow for drift time data extraction at each trap collision energy (trap CE). Ion intensities were normalized to a maximum value of 1 and the ATDs were smoothed using a Savitzky-Golay filter with a window length of 3 and a polynomial order of 2. The individual IM data were gathered to create the CIU data shown. Drift time (ms) is shown in the y-axis versus trap collision energy (V) in the x-axis. The relative intensities of the ATD distributions are denoted by a color-coded axis. CIU fingerprint plots and standard deviations were generated for three replicates using CIUSuite_stats function to quantify the reproducibility of the experiment. Comparison of 2 different CIU fingerprint plots was achieved using the CIUSuite_compare module.

3. Results:

3.1 Production of VHHs, purity and disulfide bridge homogeneity assessment. The model used in this study is the anti-HER2 VHH 11A4 to which we have added a poly-His tag at the C-terminus. This VHH has been widely described and produced in bacteria system [32]. The periplasmic localization peptide signal sequences, such as *OmpA* or *PelB,* were systematically used to direct the produced VHH in an oxidative environment for the formation of the expected disulfide bridge (see **Figure 1**, for detailed sequences of the different VHHs used). We produced the anti-HER2 VHH in *E. coli BL21(DE3)* strain with or without the alternative periplasmic peptide signal sequence, *PelB*, to evaluate its impact on the production yield compared to the classically used *OmpA* sequence, as well as on the disulfide bridge formation. The results are presented in **Figure 2**. First, we obtained about 1 to 10 mg/L of purified proteins from periplasmic (*OmpA* or *PelB*) and cytosolic expressions, respectively (**Table 1**), suggesting that the periplasmic signal sequence *PelB* from the pET20b vector does not affect the expression of VHHs. The SDS-PAGE analysis of the final products demonstrates the purity of the anti-HER2 VHH and gives some information on the disulfide bridge presence. First of all, a well-defined band with an apparent molecular weight of 14kDa is commonly observed for each preparation, confirming sample purity. As expected, the production in the periplasmic space (PS) results in a clear shift of the migration distance between non-reducing and reducing conditions and thus, indicates the presence of the disulfide bridge upon periplasmic expression, while not formed in the cytosolic space (**Cyto, Figure 2A**). To maintain both of these favourable conditions (high production yield and disulfide bridge formation), we chose to produce this VHH in the bacterial strain *Shuffle T7* (Shu) capable of protein disulfide bond formation in its cytoplasm as described for other proteins [43]. As shown in **Table 1**, the production yield of the *Shuffle T7* strain remained expectedly high (≈ 10 mg/L) compared to the cytosolic expression in the *E.coli BL21(DE3)* strain. In **Figure 2A**, however, the "Shu" gel lane does not show a significant band shift between non-reducing and reducing conditions. This NR band is more diffuse than in the cytosolic and periplasmic samples, indicating a potential mixture of disulfide bonded and non-bonded species. Alternatively, VHHs can also be expressed in inclusion bodies (IB) to increase their production yield [44]. The main downside of this approach is that this production mode necessitates subsequent refolding steps, which can affect the protein ternary structure and potentially induce undesired chemical modifications. However, these constraints are counterbalanced by a gain in production yield. We thus produced another batch of anti-HER2 VHH in *BL21(DE3)* using high expression conditions (Magic Media®). The protein was directly purified under denaturing condition (6 M guanidine) and refolded with an optional oxidation step in the presence of the redox GSSG/GSH couple. We refined the refolding process described by Dagar

et al [45] for the screen of buffers and added a preliminary oxidation step by bringing a reduced and oxidized glutathione mixture (10:1 ratio) to form the disulfide bridge. We adapted the refolding process described by Tsumoto *et al* [46] by adding high concentration of L-Arginine (1 M) during the refolding steps. Subsequent purification enabled us to isolate two refolded fractions (**Figure 2A**, lines RO and RR respectively). Markedly, these conditions led to a 10 fold production yield increase compared to the reference cytosolic conditions and thus represent a beneficial solution for the production of large amounts of the desired protein (see **Table 1** for further details). We obtained a high refolding yield of nearly 90% and 75% for the oxidized and reduced conditions, respectively. The band shift upon reduction was observed on the SDS-PAGE gel for the RO sample but not for the RR sample, indicating respectively the presence and absence of the disulfide bridge (**Figure 2A**, lines RO and RR).

Based on these trials, we also produced two other VHHs in the *Shuffle T7 E. coli* strain, namely the anti-HSA [29] and the anti-EGFR1 [25] which share a high framework sequence homology with the anti-HER2 (see **Figure 1** for sequence details). The main difference lies in the length of their CDR regions, particularly the CDR3. Contrarily to the anti-HER2 VHH, the clear migration shift observed between reducing and non-reducing gel analyses of the anti-EGFR1 VHH strongly suggested the formation of the disulfide bond (**Figure 2B**). Conversely, such a shift was not observed for the anti-HSA VHH, hypothesizing that the S-S bond was not formed under these *ad hoc* conditions (**Figure 2C**).

3.2 Size exclusion chromatography with multi-angle light scattering analysis (SEC-MALS). The disulfide bridge is an important key lock for the β-sheet stabilization of VHH structures. It can then impact the VHH recognition and affinity properties for its target. Before looking more precisely into this matter, the VHHs of the present work were all characterized by SEC-MALS in order to assess their homogeneity and size distribution under non-denaturing conditions (**Figure 3**). SEC chromatograms of anti-EGFR1 and anti-HSA VHHs displayed a unique symmetrical peak confirming sample purity and homogeneity (**Figure 3G**). All the anti-HER2 chromatograms except the RR sample also showed a unique and symmetrical elution peak (**Figures 3A, 3B, 3C, 3D** and **3F**). The RR sample evidenced a small shoulder preceding the monomeric elution peak that might be due to a dimerization of the protein (**Figure 3E**). MALS molecular weight calculations based on RI and UV signals give similar results, as summarized in **Table 2.** Although slightly over-estimated, the molecular weights calculated are in the range of the theoretical molecular weights determined from the primary sequence of each VHH.

3.3 Liquid chromatography coupled to ultraviolet absorption and to mass spectrometry (LC-UV-MS) analysis. To get a more comprehensive picture of the samples' homogeneity and purity, LC-UV-MS experiments were performed. This conventional technique affords to separate and quantify hydrophobically resolved species, before identifying them from their denatured intact mass measurements.

Anti-HER2 VHH samples were first characterized (**Figures 4A** to **4F** and **Table 3**). Periplasmic and cytoplasmic VHHs were shown to be the most homogeneous samples, LC-UV chromatograms revealing a predominant species eluted at 20.1 min (97 % abundance) or 21.3 min (86 %) which corresponds to the oxidized (14153.1 ± 0.3 Da) or the reduced form (14155.0 ± 0.1 Da) of the anti-HER2 VHH (theoretical average mass: 14155.8 Da, assuming no SS bridge and N-terminal Met), respectively (**Figures 4A** and **4B**). Interestingly, the disulfide state could also be addressed by LC because the SS bridge led to a significant hydrophobicity decrease in denatured and oxidized anti-HER2 VHH fractions (-1.2 min of retention time), potentially due to additional constraints induced in their solvent-accessible surface. This enables to separate them from denatured and reduced fractions under the baseline. Furthermore, a significant proportion of oxidized forms (13 % abundance) was also detected in the cytoplasmic sample, while reduced forms appeared to be negligible in the periplasmic sample (2 %). Finally, traces of extra-oxidation (1 %) occurring on both redox and main forms were concomitantly detected in the cytoplasmic (14170.6 ± 0.3 Da, 21.1 min) and the periplasmic sample (14169.2 ± 0.3 Da, 19.9 min). *Shu* sample appeared to be much more heterogeneous than the two previous ones (**Figures 4C** and **4F**). Indeed, a higher mixture of the abovementioned oxidized (14152.9 ± 0.2 Da, 23 % abundance) and reduced (14155.1 ± 0.2 Da, 56 %) fractions was detected at the same retention times. More preoccupying, additional variants were unexpectedly observed and associated to formylated forms of reduced (14183.0 ± 0.1 Da, 15 % abundance, 22.5 min retention time) and oxidized anti-HER2 VHHs (14181.0 ± 0.3 Da, 5 % abundance, 21.0 min), and to a hypothetical GSH adduct form of the reduced VHH (14284.1 ± 0.2 Da, 1 % abundance, 22.1 min). Such modifications were also found in RO and RR samples of similar heterogeneity (**Figures 4D** and **4E**). First of all, and similarly to periplasmic and cytoplasmic batches, a high redox homogeneity was found in each sample. Indeed, RO is mainly composed of oxidized anti-HER2 VHHs (14153.0 ± 0.2 Da, 66 % abundance) with only traces of reduced fractions (14154.9 ± 0.2 Da, 2 %) **(Figure 4D** and **Table 3)**. Conversely, RR displayed a high proportion of reduced anti-HER2 VHHs (14155.1 ± 0.2 Da, 74 %) and only traces of oxidized fractions (14153.9 ± 0.1 Da, 4 %) (**Figure 4E** and **Table 3**). However, these main redox states also included modified anti-HER2 VHH forms: extra-oxidation and formylation from RO (14168.8 ± 0.1 Da, 2% abundance and 14181.0 ± 0.3 Da, 30 %), but also from RR (14170.7 ± 0.2 Da, 2 % and 14183.1 ± 0.2 Da, 20 %), respectively. Anti-HSA and EGFR1 VHHs were next LC-UV-MS probed to be compared to anti-HER2 VHH also produced in *Shuffle T7 E. coli* (**Figures 4F, 4G** and **4H** and **Table 3**). Contrarily to anti-HER2, anti-HSA and anti-EGFR1 VHH samples appeared highly homogeneous, both from the disulfide state and the post-translational modifications (PTM) side. Indeed, LC-UV chromatogram from anti-HSA VHH sample depicted a main (89 % abundance) and a minor species (11%), eluted at 21.2 and 21.8 min, and corresponding to the free oxidized form (12990.0 ± 0.4 Da) and a hypothetical GSH adduct form (13119.2 ± 0.3 Da) of the anti-

HSA VHH (theoretical average mass: 12992.5 Da, assuming no SS bridge and a N-terminal Met), respectively (**Figure 4G** and **Table 3**). Besides behaving as a fully oxidized sample, anti-EGFR1 also showed to be PTM free, as suggested by the unique LC-UV species detected at 22.4 min and associated to the oxidized form (15295.2 ± 0.1 Da) of the anti-EGFR1 VHH (theoretical average mass: 15297.9 Da, assuming no SS bridge and N-terminal Met) (**Figure 4H** and **Table 3**). Interestingly here, hydrophobicity of oxidized and unmodified forms from these 3 denatured VHHs (HER2 < HSA < EGFR1) did not exactly follow their measured average masses (HSA < HER2 < EGFR1), suggesting a strong hydrophobic contribution of the less-conserved CDR3 domain notably between HER2 and HSA.

3.4 Binding properties analysed by surface plasmon resonance (SPR). Once the homogeneity and purity of these VHHs has been assessed, we wanted to measure the affinity of these proteins for their respective "antigens" and to compare it to already available data: anti-HER2 (1.9 nM) [30]; anti-HSA (17 nM) [29]; anti-EGFR (14 nM on cells) [47]. Surface plasmon resonance (SPR) measurements revealed that all VHHs presented a good affinity for their corresponding target with respective Kds of 11.3 nM, 4.8 nM and about 1 nM for anti-HSA, anti-EGFR1 and anti-HER2 VHHs (see **Table 4** for details, and **Figure 5** for sensorgram examples). SPR analyses also enabled to determine binding kinetics, notably the association (k_{on}) and dissociation rates (k_{off}) for each VHH. Herein, the anti-EGFR1 VHH associates more slowly with its target ($k_{on} \approx 2.10^5$ M^{-1} s^{-1}) than anti-HER2 VHH ($k_{on} \approx 4.10^6$ $M^{-1}.s^{-1}$) and anti-HSA VHH ($k_{on} \approx 8.10^5$ $M^{-1}.s^{-1}$), but also dissociated more slowly ($k_{off} \approx 9.10^{-4}$ s^{-1}) than the two others ($k_{off} \approx 4.10^{-3}$ and 9.10^{-3} s^{-1}, respectively). Interestingly, all the anti-HER2 VHHs exhibit similar k_{on} and k_{off} parameters, suggesting that in-mixture micro-heterogeneous forms previously depicted (disulfide bridge, PTMs), would not significantly modify binding properties.

3.5 Secondary structure analysis by circular dichroism. The high conservation of the immunoglobulin Vh domain scaffold is mainly based on a β-sheet stabilized by the canonical disulfide bridge, which can be easily observed by circular dichroism (CD). CD spectra were thus recorded for each VHH (**Figures 6A** and **6B**). As expected, CD spectra of the different anti-HER2 formats (**Figure 6A**), anti-HSA and anti-EGFR1 VHHs (**Figure 6B**) shared a common spectral feature characterized by a negative ellipticity signal around 210-220 nm and corresponding to a β-sheet motif. However, all anti-HER2 VHHs also displayed an additional negative signal around 230 nm, reported as a distorted β-sheet signature and representing a singular particularity of this VHH compare to the others [48]. CD data sets were next processed using BeStSel (Beta Structure Selection), an online software which enables to calculate the proportion of each secondary structure [49,50]. The results are summarized in **Table 5**. Accordingly, the anti-HSA VHH would be composed of antiparallel β-sheet (64.5 %), turn (13.5 %) and other structures (22 %). Antiparallel β-sheets would thus mostly contribute to the structure of this VHH comprising short CDR

domains (22 % of other structures) and would be subdivided into left-twisted (16 % of antiparallel β-sheet content), relaxed (35 %) and right-twisted β-sheets (49 %). Secondary structures would be more complex for anti-EGFR1 VHH due to longer CDR3 domains, but still dominated by antiparallel β-sheets (47.6 %) followed by other structures (45.6 %), turns (6 %) and α-helices (0.8 %). These results are in agreement with the crystal structure of this protein (PDB entry: 4KRN), which notably reveals a distorted α-helix inside the CDR3 loop [51] and a simulated CD spectrum matching our experimental data (data not shown). Again, the antiparallel β-sheets of the anti-EGFR1 VHH would be made of left-twisted (17.6 % of the antiparallel β-sheet structure), right-twisted (28.8 %) and relaxed β-strains (53.6 %). Anti-HER2 VHHs CD spectra clearly differed from the two others by a distorded β-sheet contribution at 230 nm. BeStSel analysis suggested that these anti-HER2 VHHs would include 58.3% of antiparallel β-sheets, 1.7 % of parallel β-sheets, 10.1 % of turns and 29.9 % of other structures. Contrary to the two other VHHs, this predicted parallel β-sheet part could explain the distortion of the β-sheet structure leading to the additional CD signal at 230 nm. The antiparallel β-sheet content would herein split into left-twisted β-strain (21.6 %), relaxed (32 %) and right twisted β-strains (46.7 %). Interestingly, anti-HSA and anti-HER2 VHHs would rather be composed of right-twisted antiparallel β-strains, while the anti-EGFR1 VHH would essentially be made of relaxed antiparallel β-strains.

3.6 Thermal stability analysis. Two orthogonal techniques were here applied to determine the thermal stability of native 3D structures from each VHH: circular dichroism and differential scanning fluorimetry (DSF), which enables to track any change of secondary structure (**Figures 6C** to **6H**) or intrinsic tryptophan fluorescence (**Figure 7**). CD spectral signatures of each VHH (signals at 217 and 232 nm for anti-HER2, 217 nm for anti-EGFR1 and 220nm for anti-HSA) were first monitored to calculate their half-denaturation temperatures (Tm) (**Table 6**). As expected, anti-HER2 VHHs enriched with the SS-forms (PS and RO, **Figures 6C, 6F** and **6I**) displayed a higher Tm (around 66 °C) than SH-enriched forms (around 55 °C for Cyto and Shu, **Figures 6D, 6E** and **6I**). This structural stability, improved by the presence of the disulfide bridge in anti-HER2 VHHs, was equivalent in the SS-enriched anti-EGFR1 VHH (Tm ≈ 66 °C, **Figure 6G** and **6I**). Unexpectedly, such stability was not found in the fully oxidized anti-HSA VHH, showing a Tm similar to those of anti-HER2 reduced forms (Tm ≈ 55 °C, **Figure 6H** and **6I**).

DSF-based stability studies evidenced two kinds of fluorescence profiles, depending on the type of VHH considered. On the one hand, the anti-HSA VHH experienced an expected fluorescence increase as function of the temperature. It translates a growing tryptophan solvent exposition due to protein denaturation (**Figure 7G**). On the other hand, for both anti-EGFR1 (**Figure 7F**) and anti-HER2 VHHs (**Figures 7A** to **7E**), a fluorescence decrease was observed as a function of the temperature. This was atypical but could be here explained by the presence of a tryptophan in the CDR2 or CDR3 loop of anti-

EGFR1 and anti-HER2 VHHs, respectively. Following this hypothesis, solvent-exposed tryptophans from CDR loops would first result in a high fluorescence signal at low temperature which would then decrease with protein aggregation upon heating. Thermal stability data thereby obtained from DSF analyses of anti-HSA and anti-EGFR1 VHHs were in line with CD results and respectively showed a Tm of about 59 °C and 68 °C (**Table 6**, **Figures 7G** and **7F**). A two-step curve of fluorescence decrease was then measured for Cyto, *Shu* and RR samples of the anti-HER2 VHH (**Figures 7B, 7C** and **7E**). The first curve was associated with the highest fluorescence drop and displayed an inflection point or Tm of around 58 °C, close to those obtained by CD on these same samples (55°C, **Figures 6D** and **6E, Table 6**). The inflection point of the second curve revealed another Tm of around 73 °C similar to those deduced from the CD analyses of fully oxidized anti-HER2 and anti-EGFR1 samples (70 and 66 °C, **Figures 6C, 6F** and **6G, Table 6**). Identification of two concomitant Tm values from the above-mentioned DSF studies was however consistent since these samples have been shown to contain a significant mixture of oxidized and reduced VHH forms (**Figure 4** and **Table 3**). Taking their respective UV proportions into account, DSF proved to be sensitive enough to unravel such redox mixtures. In contrast, PS and RO samples of the anti-HER2 VHH presented a single-step curve of fluorescence decrease, corresponding to a unique Tm of around 73 °C (**Figures 7A** and **7D**). Again, DSF data corroborated CD values (70 °C, **Table 6**) and confirmed the redox homogeneity of these two samples, mostly detected under disulfide bridged forms by LC-MS (**Figure 4** and **Table 3**).

3.7 Native mass spectrometry investigation of anti-HER2 VHH intact structures. In order to get structural insights into anti-HER2 VHHs and to better understand how the disulfide bridge can affect their native 3D structures, native MS was performed. This approach, suited to study non-covalent complexes of biomolecules in the gas phase, has also proved to be sensitive to the solvent accessible surface area (SASA) of in-solution native proteins, enabling to probe their overall folding or induced conformational changes through the charge state distribution (CSD) of their native ions [52–55]. Native MS experiments were here focused on periplasmic and cytoplasmic anti-HER2 VHH samples, previously shown to be the most homogeneous representatives of disulfide bridged or unbridged forms, respectively. MS spectra obtained in non-denaturing conditions were thus compared to those generated in denaturing conditions from these two samples (**Figure 8**). Denaturing MS analyses of infused periplasmic and cytoplasmic samples first corroborated LC-UV-MS data, leading to the single detection of the most abundant oxidized (14153.5 ± 0.1 Da) or reduced (14155.4 ± 0.1 Da) forms, respectively (**Figure 8A**). In addition to the average mass measurements, the redox state of these two denatured species could also be deduced from the isotopic distribution of their related ions (**Figure 8A inset)**. Indeed, comparing the isotopic distribution of similarly charged ions observed in denaturing MS analyses of both oxidized and reduced forms (11^+ herein), enabled to systematically evidence a 2 Da mass shift resulting from the disulfide state.

Moreover, such observations also led to notice that CSDs resulting from these two denatured redox species strongly differed: the oxidized form displayed a broad CSD shifted towards higher m/z ratios (i.e. lower charge states z, ranging from 6^+ to 12^+) and centered on the 8^+ charge state, while the reduced form exhibited a broad CSD shifted towards lower m/z ratios (i.e. higher charge states z, ranging from 6^+ to 16^+) and centered on the 13^+ charge state. These CSD differences suggest that solvent accessibility of basic residues exposed at the surface of these denatured VHHs and prone to ionisation, that is the SASA, would decrease upon SS bridging. In other words, denatured and oxidized species would display a more compact conformation (lower SASA) than denatured and reduced species, in agreement with their differences of hydrophobicity observed by LC-UV-MS. Periplasmic and cytoplasmic samples were then analysed under non-denaturing conditions by native MS (**Figure 8B**). Except from additional species linked to non-covalent and unspecific acetate adducts (+ 62 Da), oxidized and reduced forms were anew detected under the same masses (14153.4 ± 0.1 Da and 14155.3 ± 0.1 Da, respectively) and could still be differentiated using isotopic distributions of their native ions (**Figure 8B inset)**. However, CSD differences pinpointed in denaturing MS were no longer observed in native MS. Indeed, each redox species provided a similar and narrower CSD, shifted towards higher m/z ratios (i.e. lower charge states z, only ranging from 6^+ to 8^+) and centred on the 7^+ charge state. Altogether, these data first confirm that SASA of both oxidized and reduced species decrease from denaturing to native conditions, in agreement with the preservation of native-like structures [52,53,55]. But more importantly, the fact that oxidized and reduced forms share an identical CSD in native MS would mean that these two species adopt a similar native structure. Accordingly, the disulfide bridge would not significantly impact anti-HER2 VHH native folding, as suggested by the SEC-MALS and CD data.

3.8 Structural impact of the disulfide bridge in anti-HER2 VHHs assessed by native HDX-MS. An alternative method to promptly and globally probe the structural impact of the disulfide bridge in anti-HER2 VHHs was to combine native MS with hydrogen/deuterium exchange (HDX). In brief, the ability of amide hydrogens from native protein backbones to exchange with ambient deuterium typically serves as a sensor to track structural and dynamic features of protein complexes [56–58]. This property, linked to solvent accessibility and secondary structures, is commonly addressed from protein to peptide level by MS and has been widely used to decipher folding state and partner binding modes of various protein classes [59–63]. Despite less resolutive, native HDX-MS constitutes an original quench and LC-free approach to additionally probe H/D exchange of side chain labile hydrogens while circumventing potential online digestion and subsequent peptide fractionation bottlenecks [64–66]. In this context, anti-HER2 VHH represents a 127-residue protein containing a total of 243 labile hydrogens (120 on the side chains and termini, 123 on the amide backbone) in its neutral form (**Figure 1**). Since a disulfide bridge implies the loss of two exchangeable hydrogens in both cysteines side chains involved in the bridge, only deuterium

uptake differences significantly higher than 4 Da could be interpreted as the result of structural and/or dynamic changes between the two redox forms. Due to the depletion of PS sample stock, such experiments were thus performed between RO and Cyto batches, respectively shown to be mostly oxidized and reduced in LC-UV-MS (**Figure 9** and **Table 7**). Native MS analyses of unlabeled oxidized (RO, **Figure 9A**) and reduced forms (Cyto, **Figure 9D**) confirmed the detection of two single species sharing the same 7^+-centered CSD but differing from each other by 2 Da (**Table 7**, 14153.8 ± 0.3 and 14155.4 ± 0.1 Da, respectively). Extra-formylated forms were also observed in the oxidized VHH sample (**Figure 9A inset**, 14181.7 ± 0.3 Da), increasing MS spectrum heterogeneity and corroborating LC-UV-MS data. Incubating each redox form in D_2O from 1 min (**Figure 9B** and **9E**) to 1h (**Figure 9C** and **9F**) led to a significant but constant mass uptake over time (**Table 7**): unlabeled and oxidized VHH signals were shifted towards higher average masses of 14301.8 ± 2.1 (1min, **Figure 9B**) and 14302.9 ± 1.2 Da (1h, **Figure 9C**), while unlabeled and reduced VHH signals were displaced towards higher average masses of 14304.6 ± 1.0 (1 min, **Figure 9E**) and 14305.0 ± 1.3 Da (1 h, **Figure 9F**). Interestingly, this global deuterium uptake of around 150 Da, appeared limited regarding the number of available labile hydrogens (243, i.e. 62%) and did not markedly progress along the labeling time, suggesting either a rigid and tightly folded anti-HER2 VHH scaffold or in-source back exchange [65]. More importantly, no significant differences could be depicted here between average deuterium uptake curves of oxidized and reduced forms of anti-HER2 VHH (**Table 7**). Note however that any potential in-source back exchange could be here non-reproducible (since occurring on non-denatured ion species) and hide existing uptake differences, which is very unlikely and not considered here. Further comparison of isotopic distributions behind charge states of each redox form was unfortunately hampered by overlapping signals from extra-formylated forms. Altogether, these data also support a negligible effect of the disulfide bridge in the anti-HER2 VHH structure.

3.9 Gas-phase structure and stability of anti-HER2 VHHs probed by native IM-MS and CIU experiments. Another way to explore anti-HER2 VHH intact structures and investigate to which extent the disulfide bridge can affect them, consisted into coupling native MS with ion mobility (IM). This additional gas-phase dimension, enabling to separate native ions according to their charge but also to their shape, was shown to be a valuable way to assess intact conformations of proteins and their non-covalent assemblies [67–69]. As already described, native IM-MS experiments were carried out on periplasmic and cytoplasmic samples. Arrival time distributions (ATDs), corresponding here to the time spent by oxidized and reduced native ions to drift across the ion mobility cell, were pairwise compared on each common charge state (namely from 6^+ to 8^+, see **Figure 8B**) and thus used as a direct mean to compare their respective gas phase conformations (**Figure 10 A**). Indeed, for a given charge state, the more extended the native ion shape is, the more frequent its collisions with IM gas molecules are and the longer its drift time

will be. Accordingly, injecting oxidized (PS) and reduced (cyto) native ions of similar charge states in the IM cell under soft energy conditions (trap collision energy = 5 V), systematically provided similar ATDs, as shown on the 8^+ charge state with average drift times (t_D) centered on 5.62 ± 0.00 ms and 5.69 ± 0.06 ms, respectively (**Figure 10A top panel** and **Table 8**). Using an appropriate IM-MS calibration [40], these drift time values could be converted into collision cross sections ($^{TW}CCS_{N2\rightarrow He}$, as referred to in Gabelica *et al* [41]) which also showed to be similar for each charge state, as depicted between 8^+ oxidized (14.56 ± 0.04 nm^2) and reduced (14.62 ± 0.09 nm^2) native ions. Brought together, native IM-MS analyses of oxidized and reduced native ions suggest here that these two redox species would yet display a similar native conformation, in agreement with previous native MS, SEC-MALS and CD studies.

Native IM-MS can hence provide access to the global conformation of biological systems in the gas-phase but generally suffers from a limited resolution, rendering detection of subtle conformational changes tricky [70–72]. However, this instrumental bottleneck can sometimes be circumvented by monitoring ion conformations from their native state(s) to their activated state(s) through a collision induced unfolding (CIU) step performed in the gas-phase [73]. Besides giving insights into ion conformational stability, this alternative can also help to resolve two undistinguishable native conformations evolving however towards IM-distinguishable conformational intermediates and has already been applied with success to various protein complexes [74–76]. Such studies are typically led by first submitting ions to growing collisional energies in the trap cell before separating them in the IM cell. CIU experiments were thus performed on the neighbouring oxidized and reduced conformations of anti-HER2 VHH, and more particularly on their 8^+ charge state, selected on the basis of its intensity and its propensity to unfold in the gas phase (**Figures 10A middle and bottom panels, 10B** and **Table 8**). To that end, oxidized and reduced 8^+ native ions from periplasmic and cytoplasmic samples were conformationally pre-activated through a ramp of trap collision energy prior to be injected in the IM cell. Remarkably, their conformational stability profiles showed a significant divergence. Indeed, ATD of 8^+ reduced native ions quickly reacted to collisional energy (from 15 V), experiencing a fast and large transition toward higher drift times to ultimately reach (from 20 V) a t_D of 7.06 ± 0.00 ms and a corresponding $^{TW}CCS_{N2\rightarrow He}$ of 15.69 ± 0.02 nm^2 (**Figure 10A middle and bottom panels** and **Table 8**). Such a CIU-based conformational change (+7.3 % $^{TW}CCS_{N2\rightarrow He}$) was however not observed from the native conformation of 8^+ oxidized ions. Despite being shifted towards higher drift times over growing collisional energies, ATD of these ions underwent a much more limited transition. Indeed, collisional induced unfolding also started to occur at 15 V but led to an ultimate less extended conformation after 20V, as suggested by a t_D of 6.61 ± 0.00 ms and a $^{TW}CCS_{N2\rightarrow He}$ of 15.36 ± 0.02 nm^2 (+5.5 % $^{TW}CCS_{N2\rightarrow He}$) (**Figure 10A middle and bottom panel** and **Table 8**). Tridimensional representation and comparison of CIU fingerprints rendered these two distinct behaviours more concrete (**Figure 10B**). As described, 8^+ oxidized native ions appeared conformationally more stable than the

588 reduced ones, unfolding at the same collisional energy threshold (Trap CE = 15 V) but able to retain a
589 much more compact conformation ($t_D \approx 6.6$ ms) than activated reduced forms ($t_D \approx 7.1$ ms). To conclude,
590 8^+ native and PTM free ions extracted from native IM-MS and CIU analyses of RO and RR samples,
591 revealed identical native conformations and CIU fingerprints between RR and Cyto, as well as between
592 RO and PS samples (**Figure 10C**). The same native conformation was also found for 8^+ native and PTM
593 free ions generated from Shu sample while their CIU fingerprint proved here to be a perfect convolution
594 of oxidized and reduced CIU signatures (**Figure 10D**). Interestingly, relative quantifications based on
595 ATD peak areas extracted from activated conformations of oxidized and reduced species (respectively 33
596 and 67%, data not shown) in the transition CE window (20-40 V), match those deduced from LC-UV-MS
597 data (respectively 29 and 71% by only considering these two species).

598

4. Discussion:

As previously stated, VHH, the smallest functional part of camelid heavy-chain antibodies, was transformed from a Mother Nature exception into an ingenious way to address diseases [77]. As often in Research, the first steps towards new technologies, beyond the visions nourished by those discoveries on what they can be used for, are the practical considerations that are too often neglected in the first place. Because the therapeutic potential of the antibody area is immense, but also because the technical practicability forms a major obstacle, any extension of that domain towards routes that will simplify the approaches should be welcomed. The general view of the antibody therapy in oncology has been that the proteins *per se* were only a way to characterize the cancer cells in a physio-pathological environment. It was next suggested that adding one or several cytotoxic compounds to those antibodies would turn them into missile-launching cargos far more effective than previous addressing systems, using a series of proteins that might cover cancer-specific targets, such as kit [78], TIM-1 [79] or guanylyl cyclase C [80] to name only but a few. Then the complexity to obtain such large proteins in industrial quantity, to manipulate and load them, specifically and homogeneously, with cytotoxic compounds turned out to be major problems, sometimes to a point where the project was killed because of practical considerations. The rise of VHH proteins, with molecular weights in the 12 to 15 kDa range – as opposed to the 150 kDa of antibodies – renders those alternative strategies far more attractive. The benefits of those VHHs have been nicely discussed by van Bockstaele *et al* [77]. Furthermore, one can also imagine, in view of recent progresses in the chemical synthesis of proteins [81,82], that those proteins can be chemically synthesized. This opportunity would also facilitate the introduction of exotic amino acids that could be linked to cytotoxic compounds using alternative chemistry routes. We recently obtained the first synthetic anti-HER2 VHH [83], opening a route towards the possibility of using this approach to introduce orthogonal new chemistry to build armed VHHs. Too often as well, the practical evaluation of the characteristics of a given compound, such as innovative (bio)molecules is at first neglected. In the present work, we wanted to assess the technical steps required to understand the way those small proteins were produced, purified and characterized. For this, we designed a workflow that we dissected and benchmarked on three relevant VHHs raised against potential biomarkers in numerous pathologies, namely HSA, HER2 and EGFR1. This pilot study challenged here different modes of bacterial production and showed how these can impair VHH key attributes such as yield, homogeneity, structure and function. It is somewhat surprising that an area of such great potential be too often poorly characterized in terms of biophysical properties, despite beautiful biological data obtained with those objects [84–89]. Therefore, we embarked in a multi-stage characterization process during which model functional VHHs were thoroughly analyzed for their

631 homogeneity and structures. Attempts were even made to crystalize the anti-HER2 VHH without success
632 despite the 167 VHH structures deposited in the protein Data Bank.

633 Taking advantage of our passed knowledge in protein expression, we addressed the question of the
634 bacteria production of anti-HER2 VHH and set our experiments to compare its behavior with those of
635 other similar VHHs (anti-HSA and anti-EGFR1). After having shown that VHHs could be expressed at
636 high purity and quality, it seemed essential to rigorously characterize these recombinant VHHs. Indeed,
637 one should keep in mind that boosting the yield in bacterial production systems enhances the risk to
638 increase the sample heterogeneity. Despite those drawbacks, the whole scheme is amenable to an
639 industrial process, broadening the perspective to commercially propose these proteins. However, it would
640 be advised to avoid refolding strategies for big scale productions, due to potential modifications that can
641 result from such processes. LC-UV-MS experiments have revealed the heterogeneity of VHHs produced
642 in bacteria system in terms of disulfide bridge formation (anti-HER2 VHH: Shu, Cyto) and post-
643 translational modifications performed in the *Shuffle T7* strain and in IB expression system. The
644 periplasmic expression system shows one way to promote VHH production even if the yield is low
645 comparing to cytoplasmic or expression in IB.

646 As in many other domains, a rigorous quality control is required for the production of proteins aimed at
647 human treatments. As evidenced in the present study, SDS-PAGE appeared insufficient to extensively
648 assess sample purity and homogeneity. Indeed, this approach clearly confirmed the disulfide bridge
649 formation in anti-EGFR1 VHH but led to ambiguous or erroneous interpretations for anti-HER2 and anti-
650 HSA VHHs. Such information requires to be investigated with more sophisticated techniques. Among
651 those techniques, LC-UV-MS was proved to be a valuable tool not only to identify but also to quantify
652 hydrophobically fractionated species such as reduced, oxidized and modified forms of anti-HER2 VHH.
653 Thus, the main technique to observe the adequate formation of this bridge would be LC-MS. Furthermore,
654 MS offers the advantage to validate the presence of the desired product, and to assess its purity, while
655 documenting the nature of possible amino acid modifications that could have occurred along the process.

656 Many efforts have notably been made here to characterize and understand the importance of the disulfide
657 bridge in the overall VHH structure and affinity for its target. The covalent bond was proved to be a key
658 point not only to contribute to VHH folding but also to maintain its structure. Indeed, the SDS-PAGE
659 clearly indicates the presence of the disulfide bridge as it has been shown for the anti-EGFR1 VHH but it
660 could be more uncertain as for the anti-HER2 VHH or totally false as for the anti-HSA VHH and, by
661 consequence, high resolution techniques should be used to clearly characterize the sample composition.
662 This first part of the data obtained on samples produced in the *Shuffle T7* strain indicates that this bacteria
663 strain could be useful for VHH expression in a SS state (anti-HSA and anti-EGFR1 VHHs), although this

competence seems also to depend on the amino-acid sequence of the protein and could lead to additional protein modifications (anti-HER2 VHH). Altogether, these results suggest that the formation of the disulfide bridge is not only related to the oxidative environment during the expression but also to the sequence of the VHH CDRs, despite the close similarity between the three VHH frameworks presented herein. . Interestingly, no significant Kd differences were observed between the different anti-HER2 VHHs, suggesting that the presence of disulfide bridge has a negligible impact on the protein binding ability. Furthermore, the affinity constants of those VHHs were in the range of the corresponding antibodies. VHHs possess a canonical structure comprising a relatively standard scheme, with common features separated by usually 3 variable domains: CDR1, 2 and 3. Briefly, the three VHHs studied here are all composed of 8 residues for the CDR1 with a common GXTFXXF/YX pattern, a CDR2 of 7 or 8 residues with very closely related sequences and a highly variable CDR3 (**Figure 1**). Indeed, the CDR3 of the anti-HSA is only composed of 9 residues while the CDR3 of anti-HER2 and anti-EGFR1 VHHs contain 14 and 20 residues, respectively. It is obvious that those CDRs are responsible for the recognition of the "antigen", with a particular contribution of the larger and less conserved one, CDR3. Altogether, data reported in the present work suggest that these VHHs would share an overall antiparallel β-sheet structure, but that small differences in their primary sequences and notably in their CDRs, could strongly affect the torsion/orientation state of their respective antiparallel β-strain. Thus, we believe that these different contributions could be directly linked to the difference of affinity observed between the 3 VHHs and to their ability to form the framework canonical disulfide bridge in the *Shuffle T7 E.Coli* strain, especially in the case of the anti-HER2 VHH which exhibits an additional distorted β-sheet signature in its CD spectrum

In conclusion, we believe that the quality control of VHHs, whenever they are produced for research or therapeutic use, must be implemented by such means, to ensure their structural and stability properties. Altogether, native MS, HDX-MS, IM-MS and CIU studies first suggest than the disulfide bridge would not alter but strongly stabilize native conformations of anti-HER2 VHHs by covalently locking them, in line with CD and DSF-based stability data. These results also support that the production mode of oxidized and reduced anti-HER2 VHHs would not significantly hamper here their overall structures and stabilities. Finally, native IM-MS and CIU approaches demonstrated to be sensitive enough and with a high resolution capacity to semi-quantitatively address such structural properties inside mixtures of redox forms. To industrialize a VHH as a research or a therapeutic tool, it is really important to identify the contribution of the CDR sequences on the ability to produce high quantity at high quality in an industrialized process and not be only focused on the affinity of this object towards its "antigen".

5. References

[1] S. Singh, N.K. Kumar, P. Dwiwedi, J. Charan, R. Kaur, P. Sidhu, V.K. Chugh, Monoclonal Antibodies, Curr Clin Pharmacol 13 (2018) 85–99.

[2] A. Mullard, 2018 FDA drug approvals, Nat Rev Drug Discov 18 (2019) 85–89.

[3] S. Parakh, A.C. Parslow, H.K. Gan, A.M. Scott, Antibody-mediated delivery of therapeutics for cancer therapy, Expert Opin Drug Deliv 13 (2016) 401–419.

[4] M. Chodorge, A.J. Celeste, J. Grimsby, A. Konkar, P. Davidsson, D. Fairman, L. Jenkinson, J. Naylor, N. White, J.C. Seaman, K. Dickson, B. Kemp, J. Spooner, E. Rossy, D.C. Hornigold, J.L. Trevaskis, N.J. Bond, T.B. London, A. Buchanan, T. Vaughan, C.M. Rondinone, J.K. Osbourn, Engineering of a GLP-1 analogue peptide/anti-PCSK9 antibody fusion for type 2 diabetes treatment, Scientific Reports 8 (2018) 17545.

[5] A.H. Laustsen, A. Karatt-Vellatt, E.W. Masters, A.S. Arias, U. Pus, C. Knudsen, S. Oscoz, P. Slavny, D.T. Griffiths, A.M. Luther, R.A. Leah, M. Lindholm, B. Lomonte, J.M. Gutiérrez, J. McCafferty, In vivo neutralization of dendrotoxin-mediated neurotoxicity of black mamba venom by oligoclonal human IgG antibodies, Nature Communications 9 (2018) 3928.

[6] A.C. Chan, P.J. Carter, Therapeutic antibodies for autoimmunity and inflammation, Nat Rev Immunol 10 (2010) 301–316.

[7] A. Markham, Bezlotoxumab: First Global Approval, Drugs 76 (2016) 1793–1798.

[8] A.M. Scott, J.D. Wolchok, L.J. Old, Antibody therapy of cancer, Nat Rev Cancer 12 (2012) 278–287.

[9] G. Elia, T. Fugmann, D. Neri, From target discovery to clinical trials with armed antibody products, J Proteomics 107 (2014) 50–55.

[10] A. Beck, L. Goetsch, C. Dumontet, N. Corvaïa, Strategies and challenges for the next generation of antibody-drug conjugates, Nat Rev Drug Discov 16 (2017) 315–337.

[11] A. Thomas, B.A. Teicher, R. Hassan, Antibody–drug conjugates for cancer therapy, The Lancet Oncology 17 (2016) e254-e262.

[12] T.N. Iwata, C. Ishii, S. Ishida, Y. Ogitani, T. Wada, T. Agatsuma, A HER2-Targeting Antibody-Drug Conjugate, Trastuzumab Deruxtecan (DS-8201a), Enhances Antitumor Immunity in a Mouse Model, Mol Cancer Ther 17 (2018) 1494–1503.

[13] C. Szot, S. Saha, X.M. Zhang, Z. Zhu, M.B. Hilton, K. Morris, S. Seaman, J.M. Dunleavey, K.-S. Hsu, G.-J. Yu, H. Morris, D.A. Swing, D.C. Haines, Y. Wang, J. Hwang, Y. Feng, D. Welsch, G. DeCrescenzo, A. Chaudhary, E. Zudaire, D.S. Dimitrov, B. St Croix, Tumor stroma-targeted antibody-drug conjugate triggers localized anticancer drug release, J Clin Invest 128 (2018) 2927–2943.

[14] S. Cho, F. Zammarchi, D.G. Williams, C.E.G. Havenith, N.R. Monks, P. Tyrer, F. D'Hooge, R. Fleming, K. Vashisht, N. Dimasi, F. Bertelli, S. Corbett, L. Adams, H.W. Reinert, S. Dissanayake, C.E. Britten, W. King, K. Dacosta, R. Tammali, K. Schifferli, P. Strout, M. Korade, M.J. Masson Hinrichs, S. Chivers, E. Corey, H. Liu, S. Kim, N.H. Bander, P.W. Howard, J.A. Hartley, S. Coats, D.A. Tice, R. Herbst, P.H. van Berkel, Antitumor Activity of MEDI3726 (ADCT-401), a Pyrrolobenzodiazepine Antibody-Drug Conjugate Targeting PSMA, in Preclinical Models of Prostate Cancer, Mol Cancer Ther 17 (2018) 2176–2186.

[15] P. Strop, T.-T. Tran, M. Dorywalska, K. Delaria, R. Dushin, O.K. Wong, W.-H. Ho, D. Zhou, A. Wu, E. Kraynov, L. Aschenbrenner, B. Han, C.J. O'Donnell, J. Pons, A. Rajpal, D.L. Shelton, S.-H.

Liu, RN927C, a Site-Specific Trop-2 Antibody-Drug Conjugate (ADC) with Enhanced Stability, Is Highly Efficacious in Preclinical Solid Tumor Models, Mol Cancer Ther 15 (2016) 2698–2708.
[16] P. Polakis, Antibody Drug Conjugates for Cancer Therapy, Pharmacol Rev 68 (2016) 3–19.
[17] Y. Mimura, T. Katoh, R. Saldova, R. O'Flaherty, T. Izumi, Y. Mimura-Kimura, T. Utsunomiya, Y. Mizukami, K. Yamamoto, T. Matsumoto, P.M. Rudd, Glycosylation engineering of therapeutic IgG antibodies: challenges for the safety, functionality and efficacy, Protein Cell 9 (2018) 47–62.
[18] F.S. van de Bovenkamp, N.I.L. Derksen, P. Ooijevaar-de Heer, K.A. van Schie, S. Kruithof, M.A. Berkowska, C.E. van der Schoot, H. IJspeert, M. van der Burg, A. Gils, L. Hafkenscheid, R.E.M. Toes, Y. Rombouts, R. Plomp, M. Wuhrer, S.M. van Ham, G. Vidarsson, T. Rispens, Adaptive antibody diversification through N-linked glycosylation of the immunoglobulin variable region, Proc Natl Acad Sci U S A 115 (2018) 1901–1906.
[19] G. Husson, A. Delangle, J. O'Hara, S. Cianferani, A. Gervais, A. van Dorsselaer, D. Bracewell, C. Carapito, Dual Data-Independent Acquisition Approach Combining Global HCP Profiling and Absolute Quantification of Key Impurities during Bioprocess Development, Anal. Chem. 90 (2018) 1241–1247.
[20] A. Skerra, Alternative non-antibody scaffolds for molecular recognition, Curr Opin Biotechnol 18 (2007) 295–304.
[21] E.R. Goldman, J.L. Liu, D. Zabetakis, G.P. Anderson, Enhancing Stability of Camelid and Shark Single Domain Antibodies: An Overview, Front. Immunol. 8 (2017) 865.
[22] C. Vincke, S. Muyldermans, Introduction to Heavy Chain Antibodies and Derived Nanobodies, in: D. Saerens, S. Muyldermans (Eds.) Single Domain Antibodies, Humana Press, Totowa, NJ, 2012 pp. 15–26.
[23] S. Muyldermans, Nanobodies, Annu. Rev. Biochem. 82 (2013) 775–797.
[24] J. Rios-Doria, J. Harper, R. Rothstein, L. Wetzel, J. Chesebrough, A. Marrero, C. Chen, P. Strout, K. Mulgrew, K. McGlinchey, R. Fleming, B. Bezabeh, J. Meekin, D. Stewart, M. Kennedy, P. Martin, A. Buchanan, N. Dimasi, E. Michelotti, R. Hollingsworth, Antibody–Drug Conjugates Bearing Pyrrolobenzodiazepine or Tubulysin Payloads Are Immunomodulatory and Synergize with Multiple Immunotherapies, Cancer Res 77 (2017) 2686–2698.
[25] A.C. Phillips, E.R. Boghaert, K.S. Vaidya, H.D. Falls, M.J. Mitten, P.J. DeVries, L. Benatuil, C.-M. Hsieh, J.A. Meulbroek, S.C. Panchal, F.G. Buchanan, K.R. Durbin, M.J. Voorbach, D.R. Reuter, S.R. Mudd, L.I. Loberg, S.L. Ralston, D. Cao, H.K. Gan, A.M. Scott, E.B. Reilly, Characterization of ABBV-221, a Tumor-Selective EGFR-Targeting Antibody Drug Conjugate, Mol Cancer Ther 17 (2018) 795–805.
[26] D. Zhang, S.-F. Yu, S.C. Khojasteh, Y. Ma, T.H. Pillow, J.D. Sadowsky, D. Su, K.R. Kozak, K. Xu, A.G. Polson, P.S. Dragovich, C.E.C.A. Hop, Intratumoral Payload Concentration Correlates with the Activity of Antibody–Drug Conjugates, Mol Cancer Ther 17 (2018) 677–685.
[27] T.M. Cardillo, S.V. Govindan, M.B. Zalath, D.L. Rossi, Y. Wang, C.-H. Chang, D.M. Goldenberg, IMMU-140, a Novel SN-38 Antibody–Drug Conjugate Targeting HLA-DR, Mediates Dual Cytotoxic Effects in Hematologic Cancers and Malignant Melanoma, Mol Cancer Ther 17 (2018) 150–160.
[28] S. Bhakta, L.M. Crocker, Y. Chen, M. Hazen, M.M. Schutten, D. Li, C. Kuijl, R. Ohri, F. Zhong, K.A. Poon, M.A.T. Go, E. Cheng, R. Piskol, R. Firestein, A. Fourie-O'Donohue, K.R. Kozak, H. Raab, J.-A. Hongo, D. Sampath, M.S. Dennis, R.H. Scheller, P. Polakis, J.R. Junutula, An Anti-GDNF

Family Receptor Alpha 1 (GFRA1) Antibody–Drug Conjugate for the Treatment of Hormone Receptor–Positive Breast Cancer, Mol Cancer Ther 17 (2018) 638–649.
[29] R. Klooster, B.T.H. Maassen, J.C. Stam, P.W. Hermans, M.R. ten Haaft, F.J.M. Detmers, H.J. de Haard, J.A. Post, C. Theo Verrips, Improved anti-IgG and HSA affinity ligands: clinical application of VHH antibody technology, J Immunol Methods 324 (2007) 1–12.
[30] M. Kijanka, F.-J. Warnders, M. El Khattabi, M. Lub-de Hooge, G.M. van Dam, V. Ntziachristos, L. de Vries, S. Oliveira, P.M.P. van Bergen en Henegouwen, Rapid optical imaging of human breast tumour xenografts using anti-HER2 VHHs site-directly conjugated to IRDye 800CW for image-guided surgery, Eur J Nucl Med Mol Imaging 40 (2013) 1718–1729.
[31] M.M. Kijanka, A.S.A. van Brussel, E. van der Wall, W.P.T.M. Mali, P.J. van Diest, P.M.P. van Bergen en Henegouwen, S. Oliveira, Optical imaging of pre-invasive breast cancer with a combination of VHHs targeting CAIX and HER2 increases contrast and facilitates tumour characterization, EJNMMI Res 6 (2016) 109.
[32] M. Kijanka, E.G. van Donselaar, W.H. Müller, B. Dorresteijn, D. Popov-Čeleketić, M. el Khattabi, C.T. Verrips, P.M.P. van Bergen en Henegouwen, J.A. Post, A novel immuno-gold labeling protocol for nanobody-based detection of HER2 in breast cancer cells using immuno-electron microscopy, Journal of Structural Biology 199 (2017) 1–11.
[33] M. Vandesquille, T. Li, C. Po, C. Ganneau, P. Lenormand, C. Dudeffant, C. Czech, F. Grueninger, C. Duyckaerts, B. Delatour, M. Dhenain, P. Lafaye, S. Bay, Chemically-defined camelid antibody bioconjugate for the magnetic resonance imaging of Alzheimer's disease, MAbs 9 (2017) 1016–1027.
[34] J.A. Boutin, A.L. Tartar, A. van Dorsselaer, H. Vaudry, General lack of structural characterization of chemically synthesized long peptides, Protein Sci 28 (2019) 857–867.
[35] I.A. Kaltashov, C.E. Bobst, R.R. Abzalimov, G. Wang, B. Baykal, S. Wang, Advances and challenges in analytical characterization of biotechnology products: mass spectrometry-based approaches to study properties and behavior of protein therapeutics, Biotechnol Adv 30 (2012) 210–222.
[36] U. Leurs, U.H. Mistarz, K.D. Rand, Getting to the core of protein pharmaceuticals—Comprehensive structure analysis by mass spectrometry, Eur J Pharm Biopharm 93 (2015) 95–109.
[37] M. Tassi, J. de Vos, S. Chatterjee, F. Sobott, J. Bones, S. Eeltink, Advances in native high-performance liquid chromatography and intact mass spectrometry for the characterization of biopharmaceutical products, J Sep Sci 41 (2018) 125–144.
[38] P. Bannas, J. Hambach, F. Koch-Nolte, Nanobodies and Nanobody-Based Human Heavy Chain Antibodies As Antitumor Therapeutics, Front. Immunol. 8 (2017) 1603.
[39] P. Bannas, F. Koch-Nolte, Perspectives for the Development of CD38-Specific Heavy Chain Antibodies as Therapeutics for Multiple Myeloma, Front. Immunol. 9 (2018) 2559.
[40] M.F. Bush, Z. Hall, K. Giles, J. Hoyes, C.V. Robinson, B.T. Ruotolo, Collision cross sections of proteins and their complexes: a calibration framework and database for gas-phase structural biology, Anal Chem 82 (2010) 9557–9565.
[41] V. Gabelica, A.A. Shvartsburg, C. Afonso, P. Barran, J.L.P. Benesch, C. Bleiholder, M.T. Bowers, A. Bilbao, M.F. Bush, J.L. Campbell, I.D.G. Campuzano, T. Causon, B.H. Clowers, C.S. Creaser, E. de Pauw, J. Far, F. Fernandez-Lima, J.C. Fjeldsted, K. Giles, M. Groessl, C.J. Hogan, S. Hann, H.I. Kim, R.T. Kurulugama, J.C. May, J.A. McLean, K. Pagel, K. Richardson, M.E. Ridgeway,

F. Rosu, F. Sobott, K. Thalassinos, S.J. Valentine, T. Wyttenbach, Recommendations for reporting ion mobility Mass Spectrometry measurements, Mass Spectrom Rev 38 (2019) 291–320.
[42] J.D. Eschweiler, J.N. Rabuck-Gibbons, Y. Tian, B.T. Ruotolo, CIUSuite, Anal. Chem. 87 (2015) 11516–11522.
[43] J. Lobstein, C.A. Emrich, C. Jeans, M. Faulkner, P. Riggs, M. Berkmen, SHuffle, a novel Escherichia coli protein expression strain capable of correctly folding disulfide bonded proteins in its cytoplasm, Microb Cell Fact 11 (2012) 327.
[44] M. Maggi, C. Scotti, Enhanced expression and purification of camelid single domain VHH antibodies from classical inclusion bodies, Protein Expression and Purification 136 (2017) 39–44.
[45] V.K. Dagar, Adivitiya, Y.P. Khasa, High-level expression and efficient refolding of therapeutically important recombinant human Interleukin-3 (hIL-3) in E. coli, Protein Expression and Purification 131 (2017) 51–59.
[46] K. Tsumoto, M. Umetsu, I. Kumagai, D. Ejima, J.S. Philo, T. Arakawa, Role of arginine in protein refolding, solubilization, and purification, Biotechnol Prog 20 (2004) 1301–1308.
[47] R.C. Roovers, M.J.W.D. Vosjan, T. Laeremans, R. el Khoulati, R.C.G. de Bruin, K.M. Ferguson, A.J. Verkleij, G.A.M.S. van Dongen, P.M.P. van Bergen en Henegouwen, A biparatopic anti-EGFR nanobody efficiently inhibits solid tumour growth, Int J Cancer 129 (2011) 2013–2024.
[48] P. Manavalan, W.C. Johnson, Sensitivity of circular dichroism to protein tertiary structure class, Nature 305 (1983) 831–832.
[49] A. Micsonai, F. Wien, É. Bulyáki, J. Kun, É. Moussong, Y.-H. Lee, Y. Goto, M. Réfrégiers, J. Kardos, BeStSel, Nucleic Acids Res 46 (2018) W315-W322.
[50] A. Micsonai, F. Wien, L. Kernya, Y.-H. Lee, Y. Goto, M. Réfrégiers, J. Kardos, Accurate secondary structure prediction and fold recognition for circular dichroism spectroscopy, Proc Natl Acad Sci U S A 112 (2015) E3095-103.
[51] K.R. Schmitz, A. Bagchi, R.C. Roovers, P.M.P. van Bergen en Henegouwen, K.M. Ferguson, Structural Evaluation of EGFR Inhibition Mechanisms for Nanobodies/VHH Domains, Structure 21 (2013) 1214–1224.
[52] Z. Hall, C.V. Robinson, Do charge state signatures guarantee protein conformations?, J Am Soc Mass Spectrom 23 (2012) 1161–1168.
[53] I.A. Kaltashov, R.R. Abzalimov, Do ionic charges in ESI MS provide useful information on macromolecular structure?, J Am Soc Mass Spectrom 19 (2008) 1239–1246.
[54] K. Lorenzen, E. van Duijn, Native mass spectrometry as a tool in structural biology, Curr Protoc Protein Sci Chapter 17 (2010) Unit17.12.
[55] A. Natalello, C. Santambrogio, R. Grandori, Are Charge-State Distributions a Reliable Tool Describing Molecular Ensembles of Intrinsically Disordered Proteins by Native MS?, J Am Soc Mass Spectrom 28 (2017) 21–28.
[56] G.R. Masson, M.L. Jenkins, J.E. Burke, An overview of hydrogen deuterium exchange mass spectrometry (HDX-MS) in drug discovery, Expert Opin Drug Discov 12 (2017) 981–994.
[57] A.J. Percy, M. Rey, K.M. Burns, D.C. Schriemer, Probing protein interactions with hydrogen/deuterium exchange and mass spectrometry-a review, Anal Chim Acta 721 (2012) 7–21.
[58] M.J. Chalmers, S.A. Busby, B.D. Pascal, G.M. West, P.R. Griffin, Differential hydrogen/deuterium exchange mass spectrometry analysis of protein-ligand interactions, Expert Rev Proteomics 8 (2011) 43–59.

[59] G. Terral, T. Champion, F. Debaene, O. Colas, M. Bourguet, E. Wagner-Rousset, N. Corvaia, A. Beck, S. Cianferani, Epitope characterization of anti-JAM-A antibodies using orthogonal mass spectrometry and surface plasmon resonance approaches, MAbs 9 (2017) 1317–1326.
[60] N.M. Duc, Y. Du, C. Zhang, S.Y. Lee, T.S. Thorsen, B.K. Kobilka, K.Y. Chung, Effective application of bicelles for conformational analysis of G protein-coupled receptors by hydrogen/deuterium exchange mass spectrometry, J Am Soc Mass Spectrom 26 (2015) 808–817.
[61] D.P. O'Brien, B. Hernandez, D. Durand, V. Hourdel, A.-C. Sotomayor-Pérez, P. Vachette, M. Ghomi, J. Chamot-Rooke, D. Ladant, S. Brier, A. Chenal, Structural models of intrinsically disordered and calcium-bound folded states of a protein adapted for secretion, Scientific Reports 5 (2015) 14223.
[62] J. Lu, R.A. Harrison, L. Li, M. Zeng, S. Gondi, D. Scott, N.S. Gray, J.R. Engen, K.D. Westover, KRAS G12C Drug Development: Discrimination between Switch II Pocket Configurations Using Hydrogen/Deuterium-Exchange Mass Spectrometry, Structure 25 (2017) 1442-1448.e3.
[63] M.B. Trelle, D.M. Dupont, J.B. Madsen, P.A. Andreasen, T.J.D. Jørgensen, Dissecting the effect of RNA aptamer binding on the dynamics of plasminogen activator inhibitor 1 using hydrogen/deuterium exchange mass spectrometry, ACS Chem Biol 9 (2014) 174–182.
[64] V. Katta, B.T. Chait, Conformational changes in proteins probed by hydrogen-exchange electrospray-ionization mass spectrometry, Rapid Commun Mass Spectrom 5 (1991) 214–217.
[65] C.C. Going, Z. Xia, E.R. Williams, Real-time HD Exchange Kinetics of Proteins from Buffered Aqueous Solution with Electrothermal Supercharging and Top-Down Tandem Mass Spectrometry, J Am Soc Mass Spectrom 27 (2016) 1019–1027.
[66] H. Xiao, I.A. Kaltashov, Transient structural disorder as a facilitator of protein-ligand binding: native H/D exchange-mass spectrometry study of cellular retinoic acid binding protein I, J Am Soc Mass Spectrom 16 (2005) 869–879.
[67] F. Lanucara, S.W. Holman, C.J. Gray, C.E. Eyers, The power of ion mobility-mass spectrometry for structural characterization and the study of conformational dynamics, Nat Chem 6 (2014) 281–294.
[68] C. Uetrecht, R.J. Rose, E. van Duijn, K. Lorenzen, A.J.R. Heck, Ion mobility mass spectrometry of proteins and protein assemblies, Chem Soc Rev 39 (2010) 1633–1655.
[69] J. Seo, W. Hoffmann, S. Warnke, M.T. Bowers, K. Pagel, G. von Helden, Retention of Native Protein Structures in the Absence of Solvent: A Coupled Ion Mobility and Spectroscopic Study, Angew Chem Int Ed Engl 55 (2016) 14173–14176.
[70] C. Atmanene, D. Chaix, Y. Bessin, N. Declerck, A. van Dorsselaer, S. Sanglier-Cianferani, Combination of noncovalent mass spectrometry and traveling wave ion mobility spectrometry reveals sugar-induced conformational changes of central glycolytic genes repressor/DNA complex, Anal. Chem. 82 (2010) 3597–3605.
[71] C. Atmanene, S. Petiot-Bécard, D. Zeyer, A. van Dorsselaer, V. Vivat Hannah, S. Sanglier-Cianférani, Exploring key parameters to detect subtle ligand-induced protein conformational changes using traveling wave ion mobility mass spectrometry, Anal Chem 84 (2012) 4703–4710.
[72] J. Stojko, S. Fieulaine, S. Petiot-Bécard, A. van Dorsselaer, T. Meinnel, C. Giglione, S. Cianférani, Ion mobility coupled to native mass spectrometry as a relevant tool to investigate extremely small ligand-induced conformational changes, Analyst 140 (2015) 7234–7245.
[73] S.M. Dixit, D.A. Polasky, B.T. Ruotolo, Collision induced unfolding of isolated proteins in the gas phase: past, present, and future, Curr Opin Chem Biol 42 (2018) 93–100.

[74] J.N. Rabuck-Gibbons, J.E. Keating, B.T. Ruotolo, Collision induced unfolding and dissociation differentiates ATP-competitive from allosteric protein tyrosine kinase inhibitors, International Journal of Mass Spectrometry 427 (2018) 151–156.
[75] T. Botzanowski, S. Erb, O. Hernandez-Alba, A. Ehkirch, O. Colas, E. Wagner-Rousset, D. Rabuka, A. Beck, P.M. Drake, S. Cianférani, Insights from native mass spectrometry approaches for top- and middle- level characterization of site-specific antibody-drug conjugates, MAbs 9 (2017) 801–811.
[76] O. Hernandez-Alba, E. Wagner-Rousset, A. Beck, S. Cianférani, Native Mass Spectrometry, Ion Mobility, and Collision-Induced Unfolding for Conformational Characterization of IgG4 Monoclonal Antibodies, Anal Chem 90 (2018) 8865–8872.
[77] F. van Bockstaele, J.-B. Holz, H. Revets, The development of nanobodies for therapeutic applications, Curr Opin Investig Drugs 10 (2009) 1212–1224.
[78] T. Abrams, A. Connor, C. Fanton, S.B. Cohen, T. Huber, K. Miller, E.E. Hong, X. Niu, J. Kline, M. Ison-Dugenny, S. Harris, D. Walker, K. Krauser, F. Galimi, Z. Wang, M. Ghoddusi, K. Mansfield, S.T. Lee-Hoeflich, J. Holash, N. Pryer, W. Kluwe, S.A. Ettenberg, W.R. Sellers, E. Lees, P. Kwon, J.A. Abraham, S.C. Schleyer, Preclinical Antitumor Activity of a Novel Anti-c-KIT Antibody-Drug Conjugate against Mutant and Wild-type c-KIT-Positive Solid Tumors, Clin Cancer Res 24 (2018) 4297–4308.
[79] L.J. Thomas, L. Vitale, T. O'Neill, R.Y. Dolnick, P.K. Wallace, H. Minderman, L.E. Gergel, E.M. Forsberg, J.M. Boyer, J.R. Storey, C.D. Pilsmaker, R.A. Hammond, J. Widger, K. Sundarapandiyan, A. Crocker, H.C. Marsh, T. Keler, Development of a Novel Antibody-Drug Conjugate for the Potential Treatment of Ovarian, Lung, and Renal Cell Carcinoma Expressing TIM-1, Mol Cancer Ther 15 (2016) 2946–2954.
[80] K. Almhanna, T. Kalebic, C. Cruz, J.E. Faris, D.P. Ryan, J. Jung, T. Wyant, A.A. Fasanmade, W. Messersmith, J. Rodon, Phase I Study of the Investigational Anti-Guanylyl Cyclase Antibody-Drug Conjugate TAK-264 (MLN0264) in Adult Patients with Advanced Gastrointestinal Malignancies, Clin Cancer Res 22 (2016) 5049–5057.
[81] M. Bacchi, B. Fould, M. Jullian, A. Kreiter, A. Maurras, O. Nosjean, T. Coursindel, K. Puget, G. Ferry, J.A. Boutin, Screening ubiquitin specific protease activities using chemically synthesized ubiquitin and ubiquitinated peptides, Anal Biochem 519 (2017) 57–70.
[82] M. Bacchi, M. Jullian, S. Sirigu, B. Fould, T. Huet, L. Bruyand, M. Antoine, L. Vuillard, L. Ronga, L.M.G. Chavas, O. Nosjean, G. Ferry, K. Puget, J.A. Boutin, Total chemical synthesis, refolding, and crystallographic structure of fully active immunophilin calstabin 2 (FKBP12.6), Protein Sci 25 (2016) 2225–2242.
[83] L. Hartmann, T. Botzanowski, M. Galibert, M. Jullian, E. Chabrol, G. Zeder-Lutz, V. Kugler, J. Stojko, J.-M. Strub, G. Ferry, L. Frankiewicz, K. Puget, R. Wagner, S. Cianférani, J.A. Boutin, VHH characterization. Comparison of recombinant with chemically synthesized anti-HER2 VHH, Protein Sci (2019).
[84] H. Nakayama, A. Murakami, M. Yoshida, J. Muraoka, J. Wakai, N. Kenjyou, Y. Ito, Characterization and Selection of 3-(1-Naphthoyl)-Indole Derivative-Specific Alpaca VHH Antibodies Using a Phage Display Library, Monoclon Antib Immunodiagn Immunother 35 (2016) 231–234.

[85] J.L. Liu, L.C. Shriver-Lake, D. Zabetakis, G.P. Anderson, E.R. Goldman, Selection and characterization of protective anti-chikungunya virus single domain antibodies, Mol Immunol 105 (2019) 190–197.
[86] G. Hussack, S. Raphael, M.J. Lowden, K.A. Henry, Isolation and characterization of camelid single-domain antibodies against HER2, BMC Res Notes 11 (2018) 866.
[87] S. Wöll, C. Bachran, S. Schiller, M. Schröder, L. Conrad, R. Scherließ, L.K. Swee, Sortagging of liposomes with a murine CD11b-specific VHH increases in vitro and in vivo targeting specificity of myeloid cells, Eur J Pharm Biopharm 134 (2019) 190–198.
[88] F. Faraji, N. Tajik, M. Behdani, M.A. Shokrgozar, A.H. Zarnani, F. Shahhosseini, M. Habibi-Anbouhi, Development and characterization of a camelid single-domain antibody directed to human CD22 biomarker, Biotechnology and Applied Biochemistry 65 (2018) 718–725.
[89] L. Schoonaert, L. Rué, B. Roucourt, M. Timmers, S. Little, L. Chávez-Gutiérrez, M. Dewilde, P. Joyce, A. Curnock, P. Weber, J. Haustraete, G. Hassanzadeh-Ghassabeh, B. de Strooper, L. van den Bosch, P. van Damme, R. Lemmens, W. Robberecht, Identification and characterization of Nanobodies targeting the EphA4 receptor, J Biol Chem 292 (2017) 11452–11465.

968

969 **Table 1: VHH production and refolding yields from the different bacterial expression systems**
970 **evaluated.**

971

Sample name	Bacteria strain/ Production localization	Production Yield (mg/L of culture)	Refolding process yield (%)
Anti-HER2 PS	*E.coli BL21(DE3)*/Periplasmic	≈1	ND
Anti-HER2 Cyto	*E.coli BL21(DE3)*/Cytosolic	≈10	ND
Anti-HER2 Shu	*E.coli Shuffle T7*/Cytosolic	≈10	ND
Anti-HER2 RO	*E.coli BL21(DE3)*/Cytosolic	≈100	≈90
Anti-HER2 RR	*E.coli BL21(DE3)*/Cytosolic	≈100	≈75
Anti-EGFR	*E.coli Shuffle T7*/Cytosolic	≈10	ND
Anti-HSA	*E.coli Shuffle T7*/Cytosolic	≈10	ND

972

973

974 **Note**: ND: not determined

975

976 **Table 2: SEC-MALS analysis**

977

Sample name	Injected mass (µg)	Mass recovery (%)	Mw (Da)
Anti-HER2 PS	21.60	88.8	14500 ± 195
Anti-HER2 Cyto	18.80	103.9	14730 ± 334
Anti-HER2 Shu	21.60	95.6	14670 ± 223
Anti-HER2 RO	17.40	101.5	14930 ± 397
Anti-HER2 RR	21.60	80.1	14630 ± 182
Anti-EGFR	19.00	104.1	15450 ± 329
Anti-HSA	21.60	92.3	13730 ± 547

978

979

980

981

982

Table 3: Relative UV quantification and MS assignment of VHH species revealed by LC-UV-MS.

Species		▲	▲‡	●	●†	●‡	○	○†	○‡	○‡	■
Measured average mass (Da)		12990.0 ± 0.4	13119.2 ± 0.3	14153.1 ± 0.3	14169.2 ± 0.3	14181.0 ± 0.3	14155.0 ± 0.1	14170.6 ± 0.3	14183.0 ± 0.1	14284.1 ± 0.2	15295.2 ± 0.1
Assignation		oxidized VHH (HSA)	GSH linked forms?	oxidized VHH (HER2)	extra oxidized forms	formylated forms	reduced VHH (HER2)	extra oxidized forms	formylated forms	GSH linked forms?	oxidized VHH (EGFR1)
Retention time (min)		21.2	21.8	20.1	19.9	21.0	21.3	21.1	22.5	22.1	22.4
Relative UV abundance (%)	PS			97	1		2				
	Cyto			13			86	1			
	Shu			23		5	56		15	1	
	RO			66	2	30	2				
	RR			4			74	2	20		
	HSA	89	11								
	EGFR1										100

988

989 **Table 4: Binding kinetics analysed by Surface Plasmon Resonance**

990

	kon± SD (M^{-1} s^{-1}) E^{+6}	koff± SD (s^{-1}) E^{-3}	Kd ± SD (nM)
Anti-HER2 PS	5.39 ± 0.13	4.85 ± 0.13	0.9 ± 0.00
Anti-HER2 Cyto	4.54 ± 0.05	2.77 ± 0.01	0.6 ± 0.00
Anti-HER2 Shu	3.83 ± 0.03	4.01 ± 0.00	1.05 ± 0.01
Anti-HER2 RO	3.05 ± 0.01	4.29 ± 0.12	1.4 ± 0.04
Anti-HER2 RR	3.35 ± 0.06	2.5 ± 0.03	0.7 ± 0.00
Anti-EGFR1	0.20 ± 0.01	0.98 ± 0.00	4.8 ± 0.03
Anti-HSA	0.81 ± 0.03	9.22 ± 0.22	11.3 ± 0.2

991

Table 5: CD spectra-derived secondary structures of the studied VHHs.

VHHs	Helix	Helix1 (regular)	Helix2 (distorted)	Antiparallel	Anti1 (left twisted)	Anti2 (relaxed)	Anti3 (right twisted)	Parallel	Turn	Others
Anti-HSA	0	0	0	64.5	10	22.8	31.7	0	13.5	22
Anti-HER2	0	0	0	58.3	12.6	18.6	27.2	1.7	10.1	29.9
Anti-EGFR1	0.8	0	0.8	47.6	8.4	25.5	13.7	0	6	45.6

Note: Proportions of each secondary structure were determined from the CD spectra using the BeStSel online software. The values in brackets correspond to the percentage of the anti1, anti2 and anti3 structure normalized to 100% of antiparallel structure.

Table 6: Tm calculation by CD and OPTIM.

	Tm by CD (°C)	Tm1 by OPTIM with ratio 350/330 nm (°C)	Tm2 by OPTIM with ratio 350/330 nm (°C)
Anti-HER2 PS	70.10 ± 0.21	73.22 ± 0.3	*
Anti-HER2 Cyto	55.09 ± 0.42	56.04 ± 0.17	72.82 ± 0.62
Anti-HER2 Shu	54.93 ± 0.58	56.09 ± 0.16	73.24 ± 1.29
Anti-HER2 RO	70.04 ± 0.18	72.15 ± 0.2	*
Anti-HER2 RR	ND	54.06 ± 0.23	*
Anti-EGFR1	65.50 ± 0.46	67.63 ± 0.32	*
Anti-HSA	54.63 ± 0.3	59.01 ± 0.43	*

Note: * No second Tm was observed. ND: not determined

Table 7: Deuterium uptake of oxidized and reduced anti-HER2 VHHs monitored by native HDX-MS.

Samples		RO		Cyto	
Native species		●	●	○	○
Assignation		Undeuterated oxidized VHH	Deuterated oxidized VHH	Undeuterated reduced VHH	Deuterated reduced VHH
Measured average mass (Da)	t_0 (unlabeled)	14153.8 ± 0.3		14155.4 ± 0.1	
	t_{1min} (D_2O label)		14301.8 ± 2.1		14304.6 ± 1.0
	t_{1hr} (D_2O label)		14302.9 ± 1.2		14305.0 ± 1.3

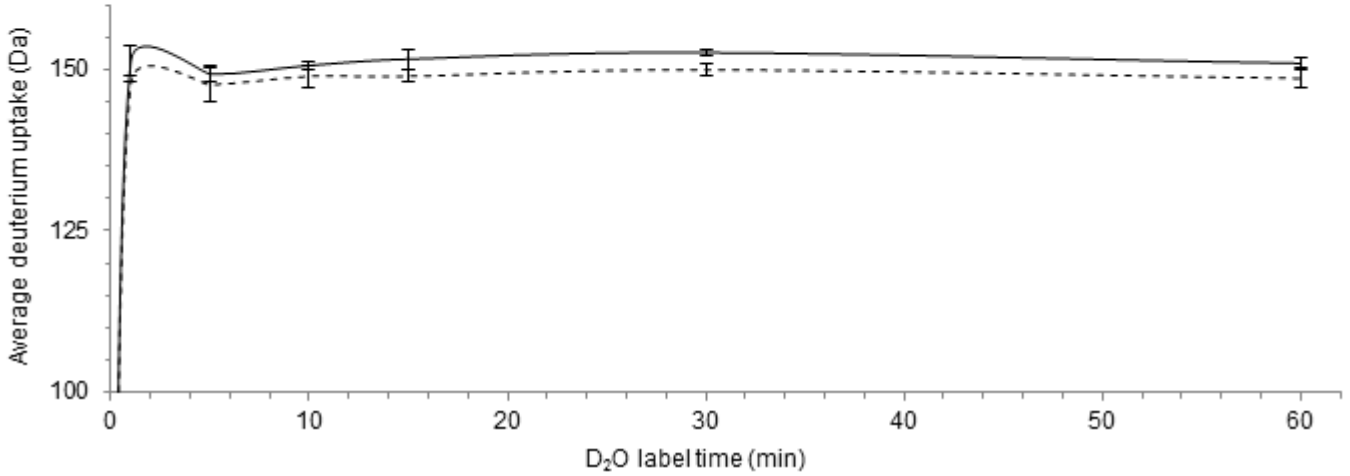

Average deuterium uptakes of oxidized (RO sample) and reduced (Cyto sample) native forms of anti-HER2 VHHs are plotted over label time as dashed and solid curves, respectively. Standard deviations displayed represent the experimental variability from sample triplicates for each label time.

Table 8: Conformational characterization of oxidized and reduced 8^+ ions under native and activated states by IM-MS.

8^+ charge state	**Reduced VHH**		**Oxidized VHH**	
Conformer				
t_D (ms)	5.69 ± 0.06	7.06 ± 0.00	5.62 ± 0.00	6.61 ± 0.00
$^{TW}CCS_{N2\rightarrow He}$ (nm^2)	14.62 ± 0.09	15.69 ± 0.02	14.56 ± 0.04	15.36 ± 0.02
$\Delta^{TW}CCS_{N2\rightarrow He}$ (%)	ref.	+7.3	ref.	+5.5

Note: $^{TW}CCS_{N2\rightarrow He}$ values of native reduced and oxidized conformations (open and filled circles, respectively) serve here as references (ref.) to express corresponding $^{TW}CCS_{N2\rightarrow He}$ increases (%) upon gas-phase activation.

Legends to the figures:

Figure 1: Sequence alignment of anti-HSA, anti-HER2 and anti-EGFR1 VHHs.

Figure 2: SDS-Page 4-12% in MES buffer of anti-HER2 VHH samples (A), anti-EGFR1 VHH sample (B) and anti-HSA VHH sample (C) in non-reducing (NR) and reducing (R) conditions. NR conditions result in the addition of idoacetamine in the LDS buffer (Invitrogen) while the sample was boiled 2 minutes at 55°C. R conditions correspond to the addition of 50 mM DTT in the LDS buffer while the sample was boiled 5 minutes at 95°C.

Figure 3: SEC-MALS chromatograms of the anti-HER2 VHH samples (A, B, C, D and E), anti-EGFR1 and anti-HSA VHH (F, G) samples. Chromatograms of the different anti-HER2 VHH samples are showed in the panel A, B, C, D and E for the PS, Cyto, Shu, RO and RR samples respectively. The panel F shows the alignment of all anti-HER2 VHH sample chromatograms with in black line the PS, in dot line the Cyto, in blue line the Shu, in red line the RO and in green line the RR sample. In the panel G, the anti-EGFR1 chromatogram is represented in black line and the anti-HSA chromatogram in dot line. The X axis represents the elution time and the Y axis is expressed in a relative scale of the UV signal at 280 nm.

Figure 4: VHHs redox state and microheterogeneity assessed by LC-UV-MS. RPLC-UV chromatograms at 280nm of denatured anti-HER2 VHH samples (A-F), anti-HSA (G) and anti-EGFR1 VHH samples (H). A: PS; B: Cyto; C and F: Shu; D: RO; E: RR. Filled and open symbols respectively indicate oxidized (SS) and reduced (SH) forms of anti-HER2 (circle), anti-HSA (triangle) and anti-EGFR1 (square) VHHs. Simple, double and triple crosses correspond to extra-oxidized, formylated and GSH-linked forms, respectively.

Figure 5: SPR sensorgrams of anti-HER2, anti-EGFR1 and anti-HSA VHH samples. Anti-HER2 VHH sensorgrams of the PS, Cyto, Shu, RO and RR samples are showed in the panel A, B, C, D and E,

respectively. Anti-EGFR1 and anti-HSA VHH sensorgrams are represented in the panel F and G, respectively. Each curve corresponds to the kinetic of one concentration from 0.122 nM to 62.5 nM for the PS, Cyto, RO and RR samples; from 0.17 nM to 40 nM for the Shu sample; from 0.195 nM to 100 nM for the anti-EGFR1 VHH sample and from 0.39 nM to 200 nM for the anti-HSA VHH sample. The PS, Cyto, RO and RR samples were injected during 4 min while the Shu, anti-EGFR1 and anti-HSA VHH samples were injected during 6 min. The dissociation time was 15 minutes for all samples excepted for the anti-EGFR1 where the dissociation time was done during 30 minutes. Experiments were performed in three concentration series starting from the lowest to the highest concentration but two series are showed in the figure. The X axis represents the time and the Y axis the response in RU.

Figure 6: Circular dichroism spectra of the VHHs. Effect of the temperature. A: PS sample in black, Cyto in red, Shu in green and RO in blue. B: anti-EGFR1 and anti-HSA VHH samples are represented in black line and in dot line, respectively. CD spectra as a function of the temperature are showed in the panel C, D, E, F, G and H for the PS, Cyto, Shu, RO, anti-EGFR1 and anti-HSA VHH samples, respectively. Each spectrum corresponds to one temperature from 25°C to 85°C. The panel I represents the CD value in mdeg at 217 nm for the anti-HER2 (PS in black, Cyto in red, Shu in green and RO in blue) and anti-EGFR1 VHHs (in orange) and at 220 nm for the anti-HSA VHH (in cyan). From these curves, the Tm of each sample was calculated using the following equation with Prism software: Y=Bottom + (Top-Bottom)/(1+10^(X-Tm)).

Figure 7: Intrinsic fluorescence of the VHHs as a function of the temperature. DSF experiments of anti-HER2 VHH samples are showed in the panel A, B, C, D and E for the PS, Cyto, Shu, RO and RR samples, respectively. DSF experiments of anti-EGFR1 and anti-HSA VHHs are represented in the panel F and G, respectively. The X-axis represents the temperature and the Y-axis the fluorescence ratio at 350 and 330 nm. Each experiment was performed in triplicate and the bars represent the error of the measurement for each point.

Figure 8: Impact of the disulfide bridge on the anti-HER2 VHH SASA probed by denaturing and native MS. Denaturing (A) and native ESI-MS spectra (B) obtained from SS (top panel, PS sample) and SH-enriched forms (bottom panel, Cyto sample) of anti-HER2 VHH under infusion. Filled and open circles respectively mark oxidized (SS) and reduced (SH) charge state distributions of anti-HER2 VHH. Insets provide a zoom on a common charge state observed in denaturing (11^+) and native (7^+) conditions. * indicate non-covalent acetate adducts (+ 62 Da).

Figure 9: Impact of the disulfide bridge on the anti-HER2 VHH SASA probed by native HDX-MS. Native ESI-MS spectra obtained from oxidized (A-C, RO sample) and reduced (D-F, Cyto sample) anti-HER2 VHHs in absence of D_2O (A,D) and after a D_2O incubation of 1 minute (B,E) and 1 hour (C,F). Filled and open circles respectively indicate oxidized (SS) and reduced (SH) forms of anti-HER2 VHH. Black and orange coloured circles mark undeuterated and deuterated species. Double crosses correspond to extra-formylated forms. Insets provide a zoom on the common native charge state 7^+ observed in undeuterated and deuterated conditions.

Figure 10: Impact of the disulfide bridge on the anti-HER2 VHH conformational stability probed by native IM-MS and collision-induced unfolding. A: Arrival time distributions of oxidized (dashed curves and filled symbols, PS sample) and reduced (solid curves and open symbols, Cyto sample) 8^+ charge states extracted from native IM-MS analyses upon various Trap collisional energies: 5V (top panel), 15 V (middle panel) and 60V (bottom panel). Symbols shape conceptualizes changes occurring in oxidized and reduced 8^+ ions conformation along gas-phase activation. B, C: Comparison of CIU fingerprints obtained between 8^+ native charge states from B Cyto (left, mostly reduced) and PS (right, mostly oxidized) samples, C RR (left, mostly reduced) and RO (right, mostly oxidized) samples. d) CIU fingerprint obtained from 8^+ native charge state of Shu sample (mixture of reduced and oxidized forms).

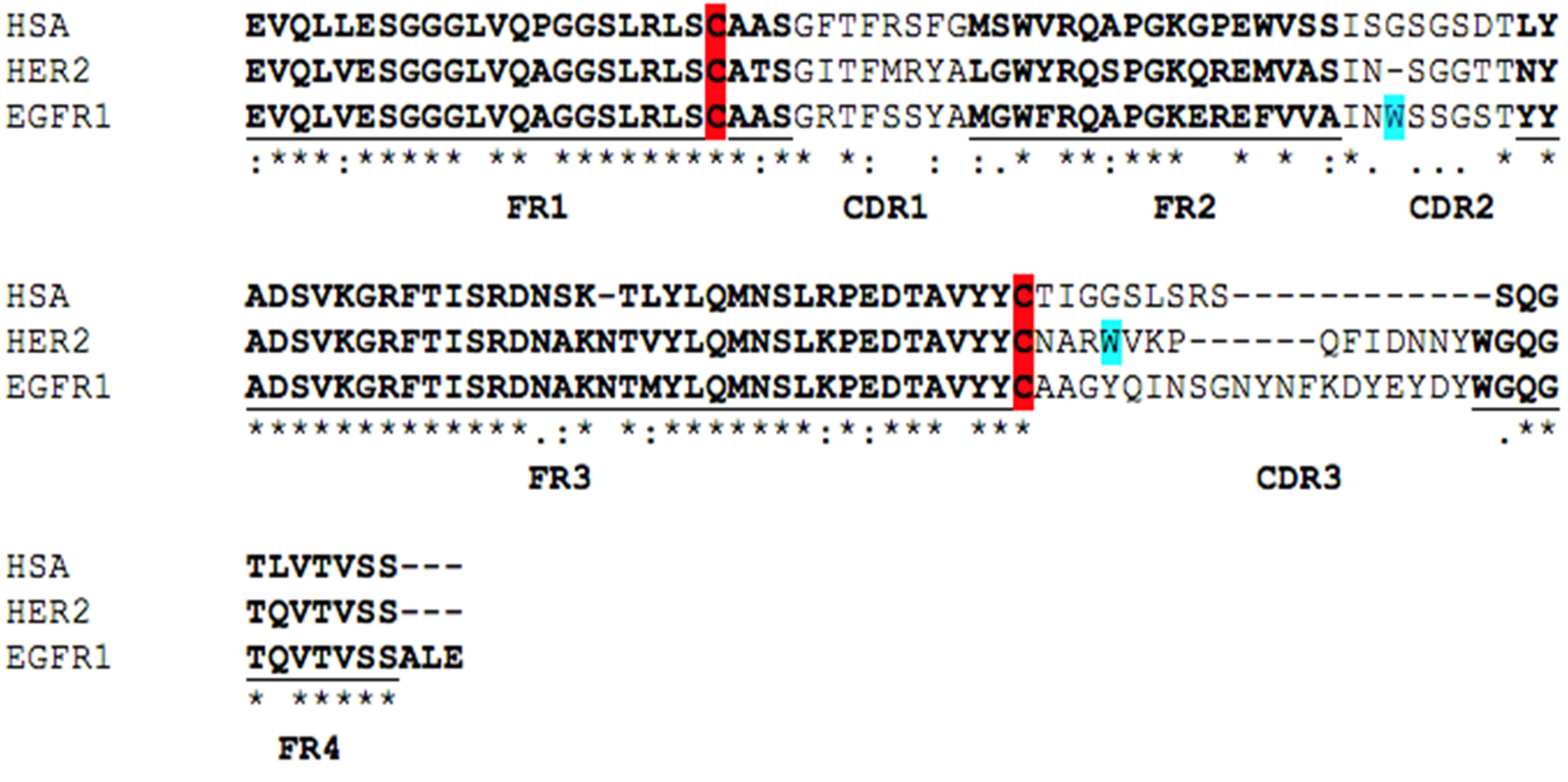
HSA EVQLLESGGGLVQPGGSLRLSCAASGFTFRSFGMSWVRQAPGKGPEWVSSISGSGSDTLY
HER2 EVQLVESGGGLVQAGGSLRLSCATSGITFMRYALGWYRQSPGKQREMVASIN-SGGTTNY
EGFR1 EVQLVESGGGLVQAGGSLRLSCAASGRTFSSYAMGWFRQAPGKEREFVVAINWSSGSTYY
FR1
CDR1
FR2
CDR2
HSA ADSVKGRFTISRDNSK-TLYLQMNSLRPEDTAVYYCTIGGSLSRS----------SQG
HER2 ADSVKGRFTISRDNAKNTVYLQMNSLKPEDTAVYYCNARWVKP------QFIDNNYWGQG
EGFR1 ADSVKGRFTISRDNAKNTMYLQMNSLKPEDTAVYYCAAGYQINSGNYNFKDYEYDYWGQG
FR3
CDR3
HSA TLVTVSS---
HER2 TQVTVSS---
EGFR1 TQVTVSSALE
FR4

Figure 1

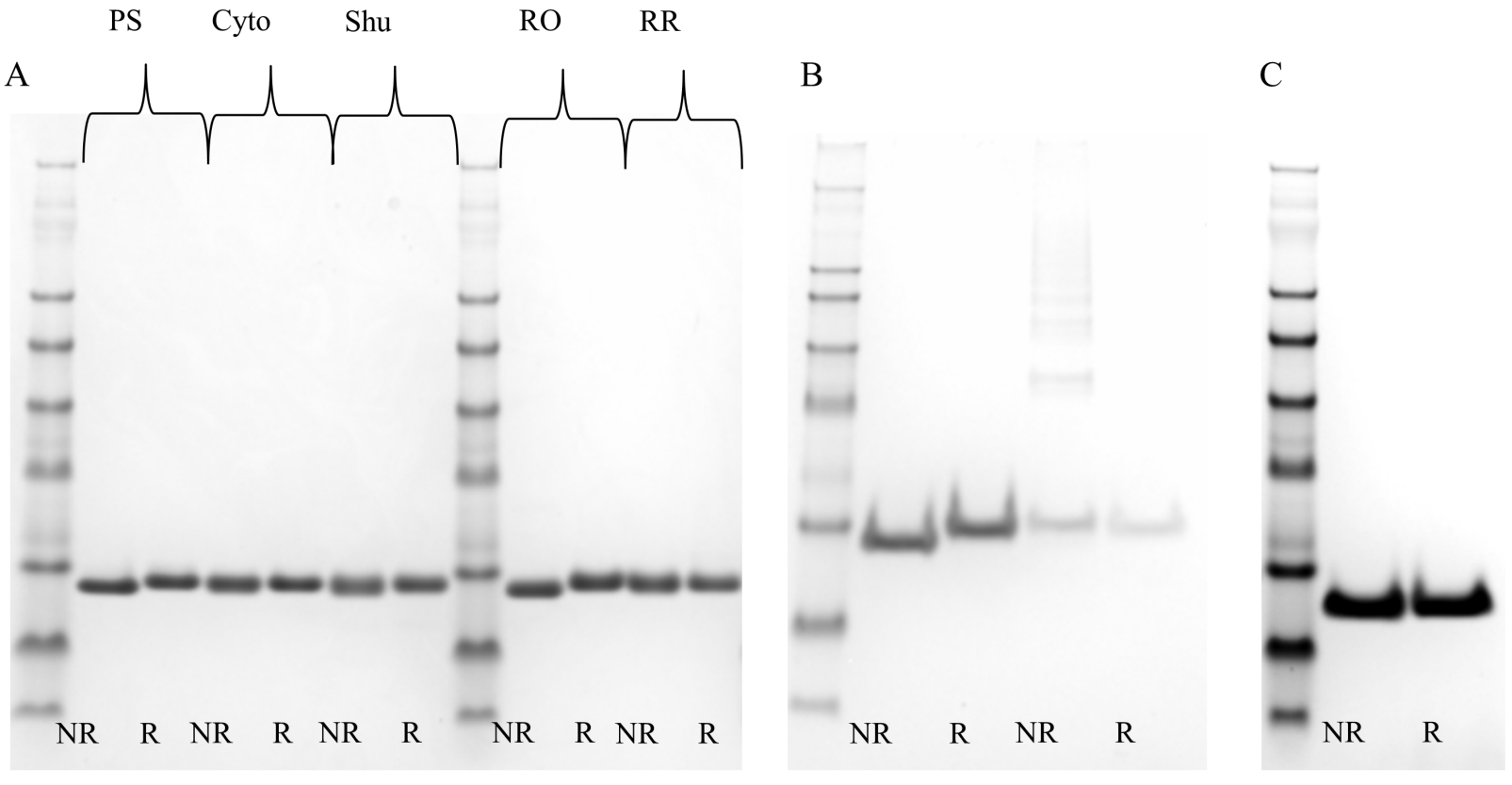

Figure 2

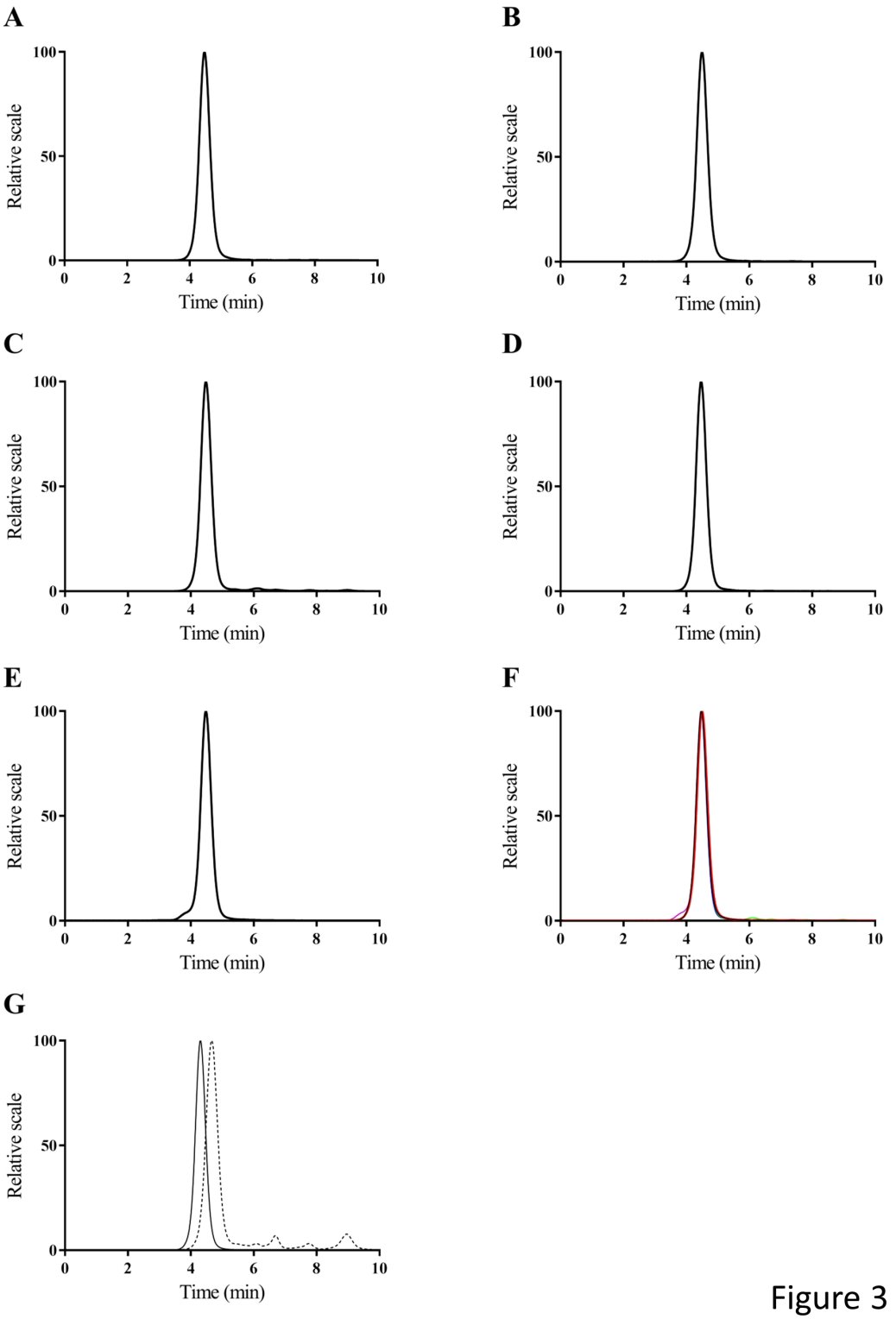

Figure 3

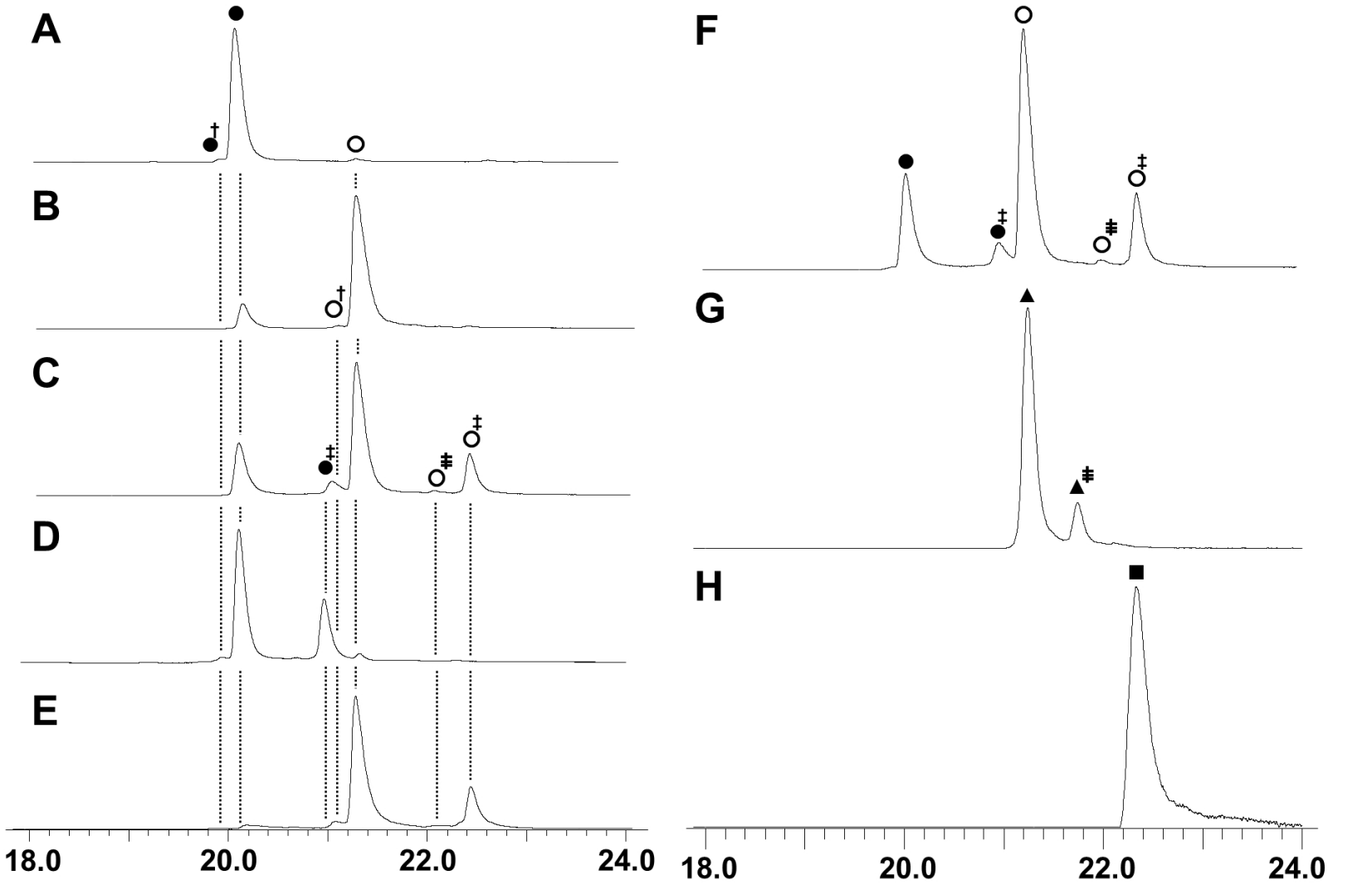

Figure 4

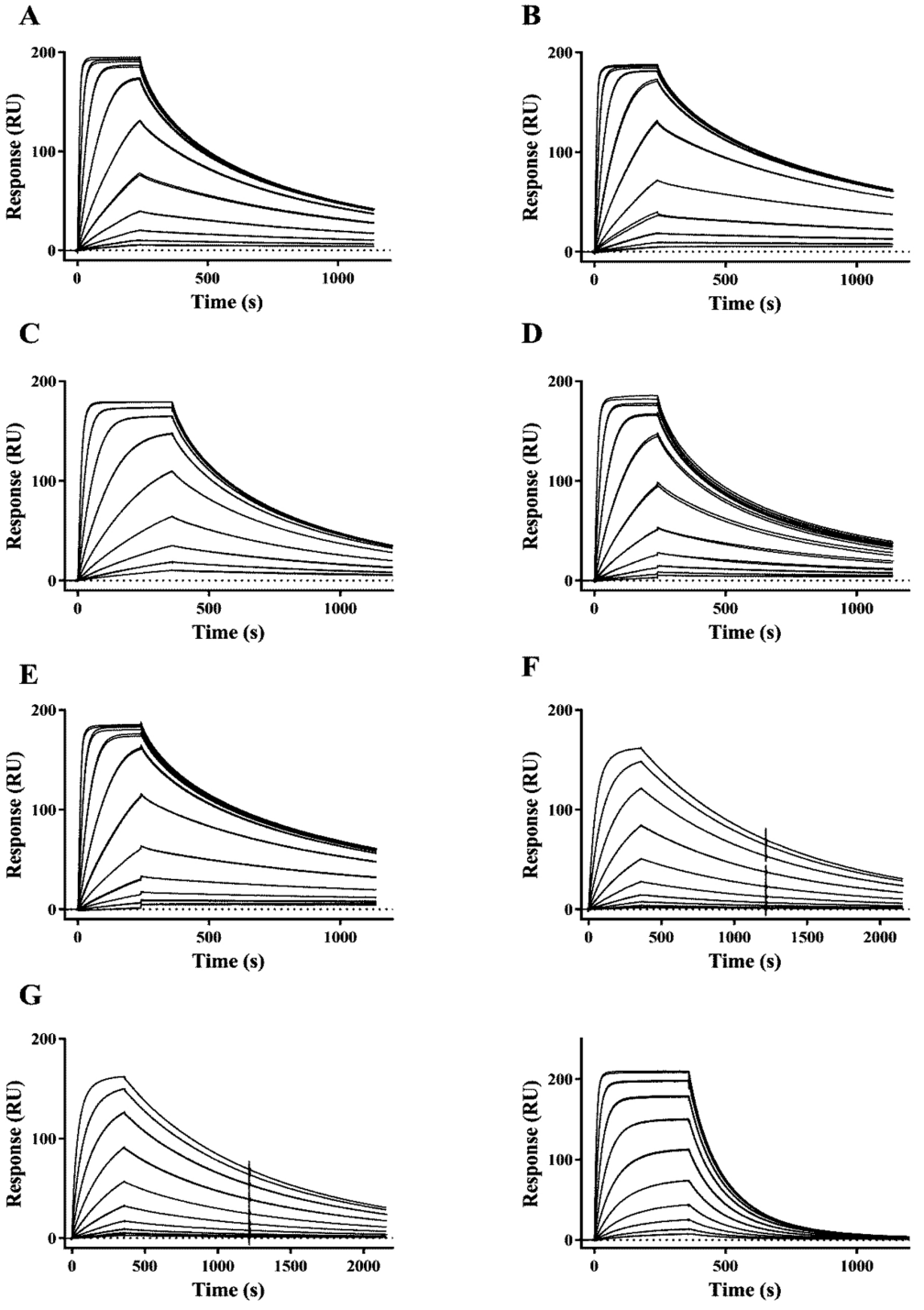

Figure 5

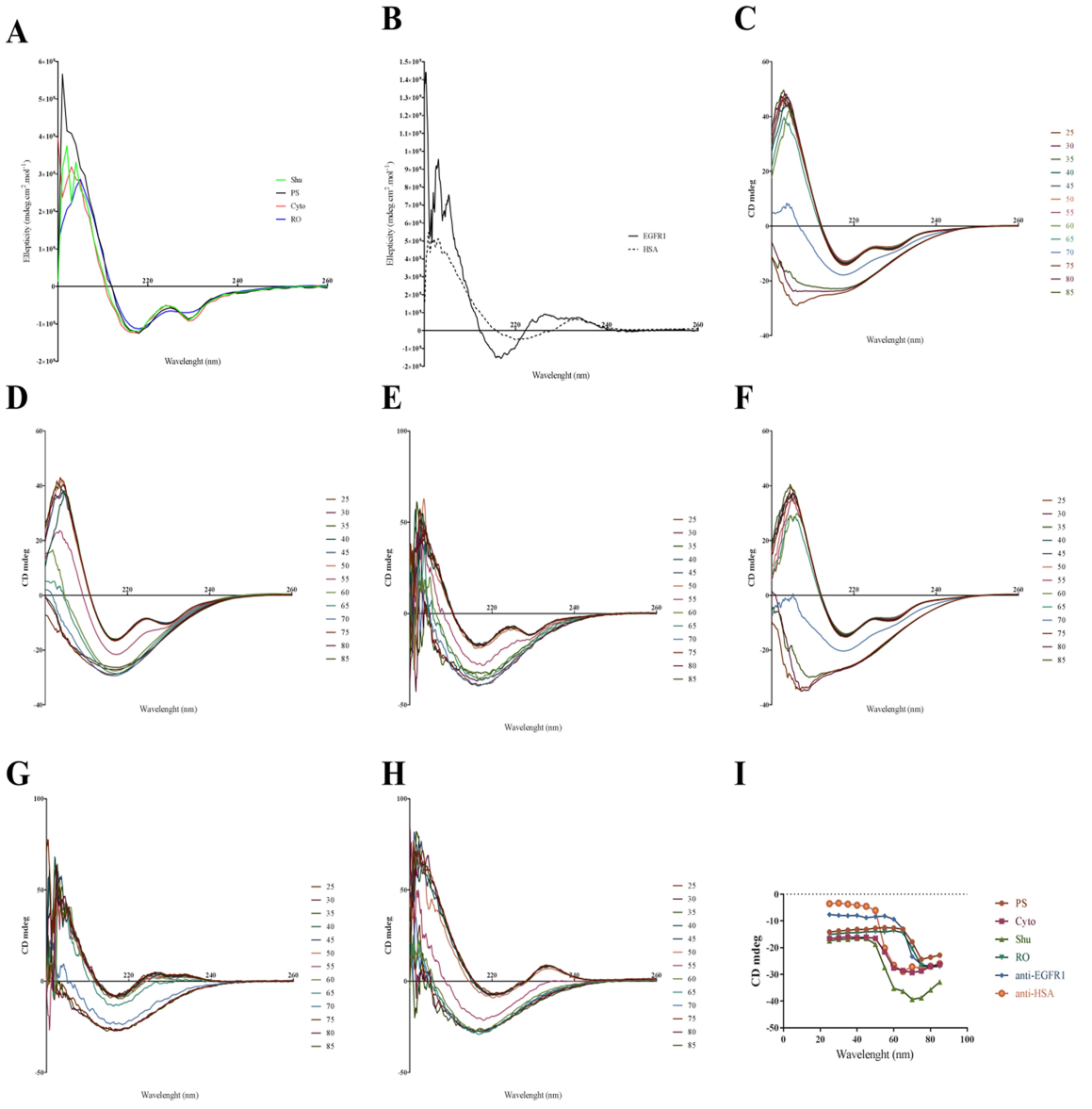
A
B
C
D
E
F
G
H
I
Ellipticity (mdeg.cm².mol⁻¹)
Wavelenght (nm)
Shu
PS
Cyto
RO
EGFR1
HSA
CD mdeg
25
30
35
40
45
50
55
60
65
70
75
80
85
anti-EGFR1
anti-HSA

Figure 6

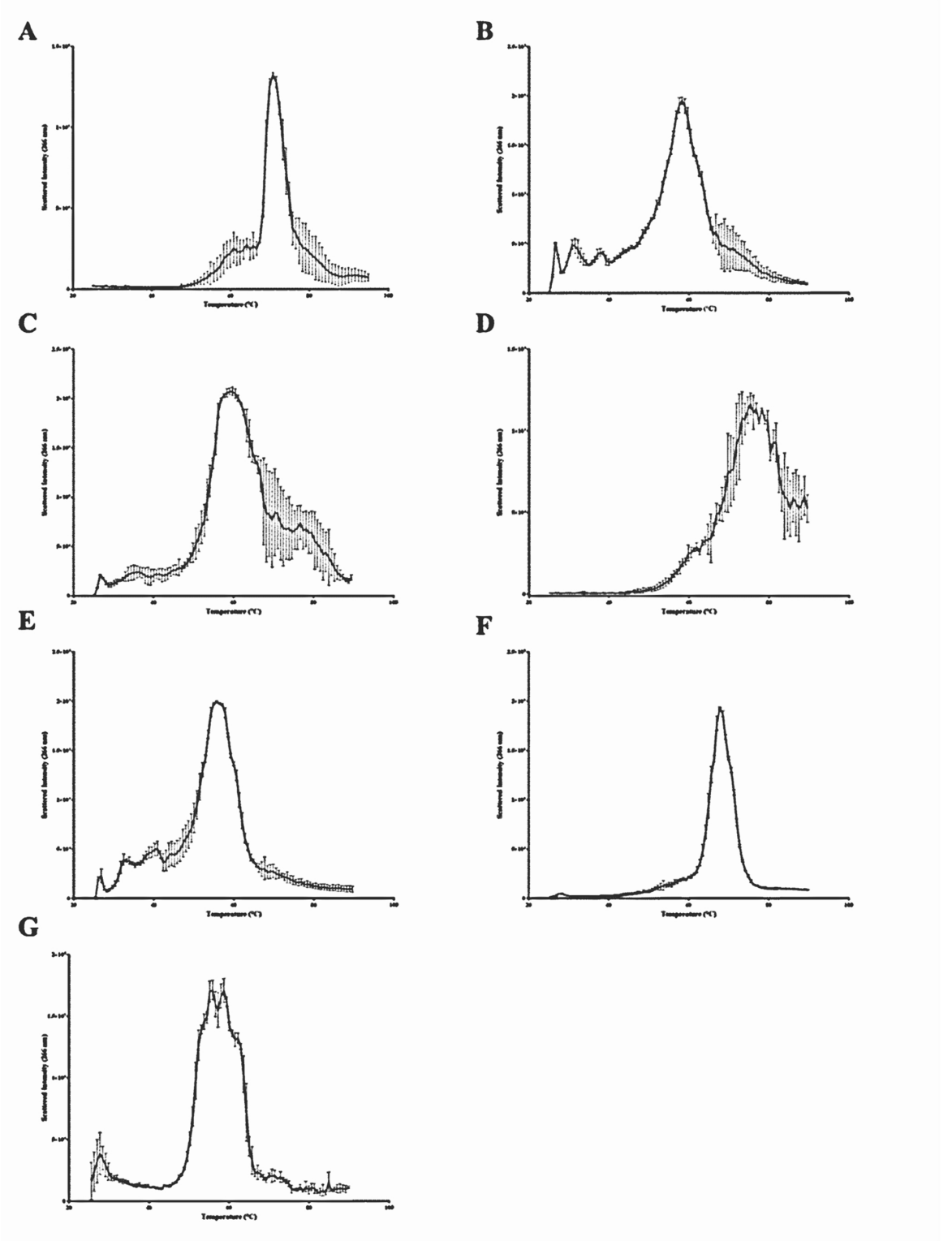

Figure 7

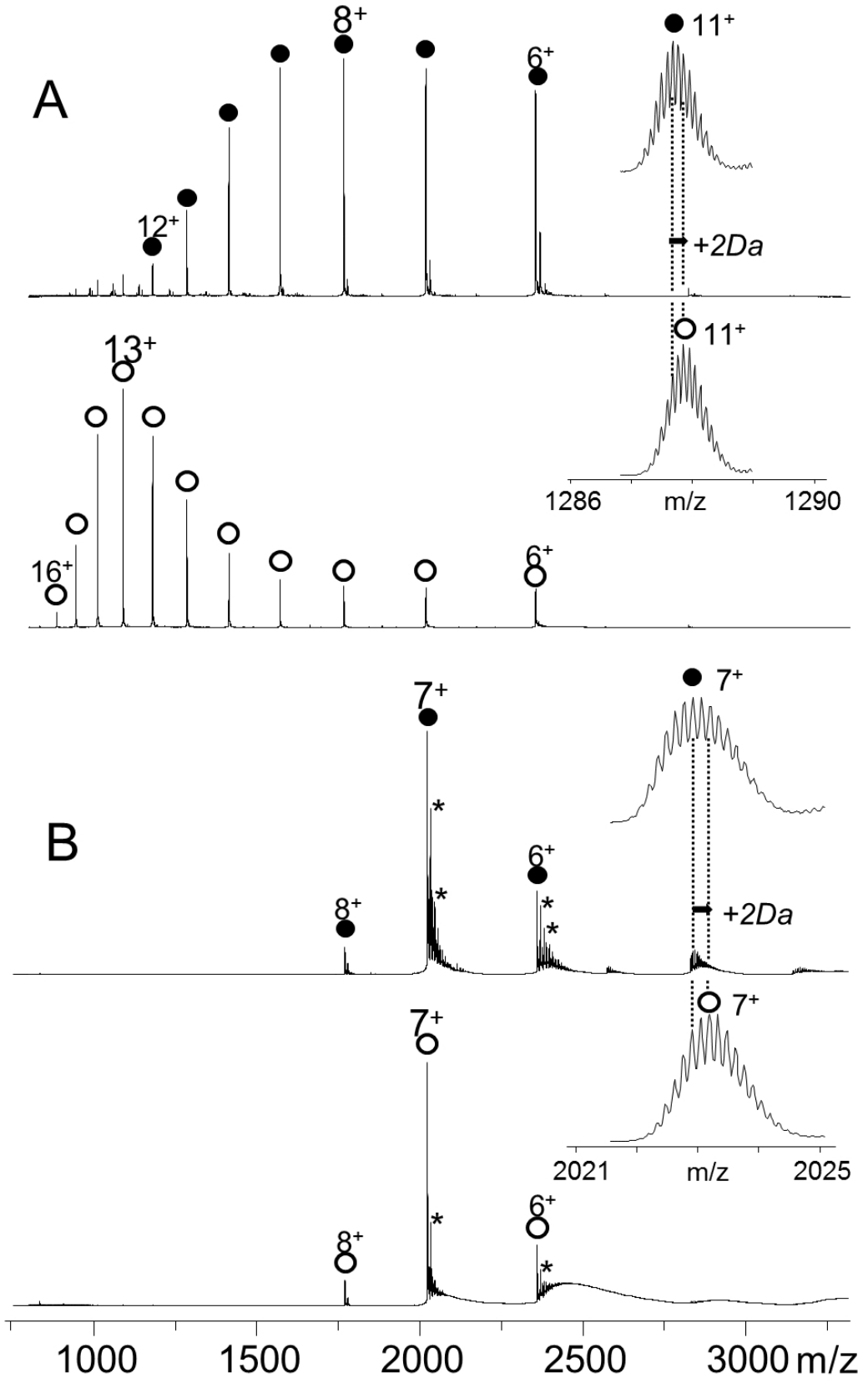
A
8+
6+
11+
12+
+2Da
11+
13+
1286
m/z
1290
16+
6+
B
7+
7+
*
6+
8+
+2Da
7+
7+
2021
m/z
2025
6+
8+
1000
1500
2000
2500
3000 m/z

Figure 8

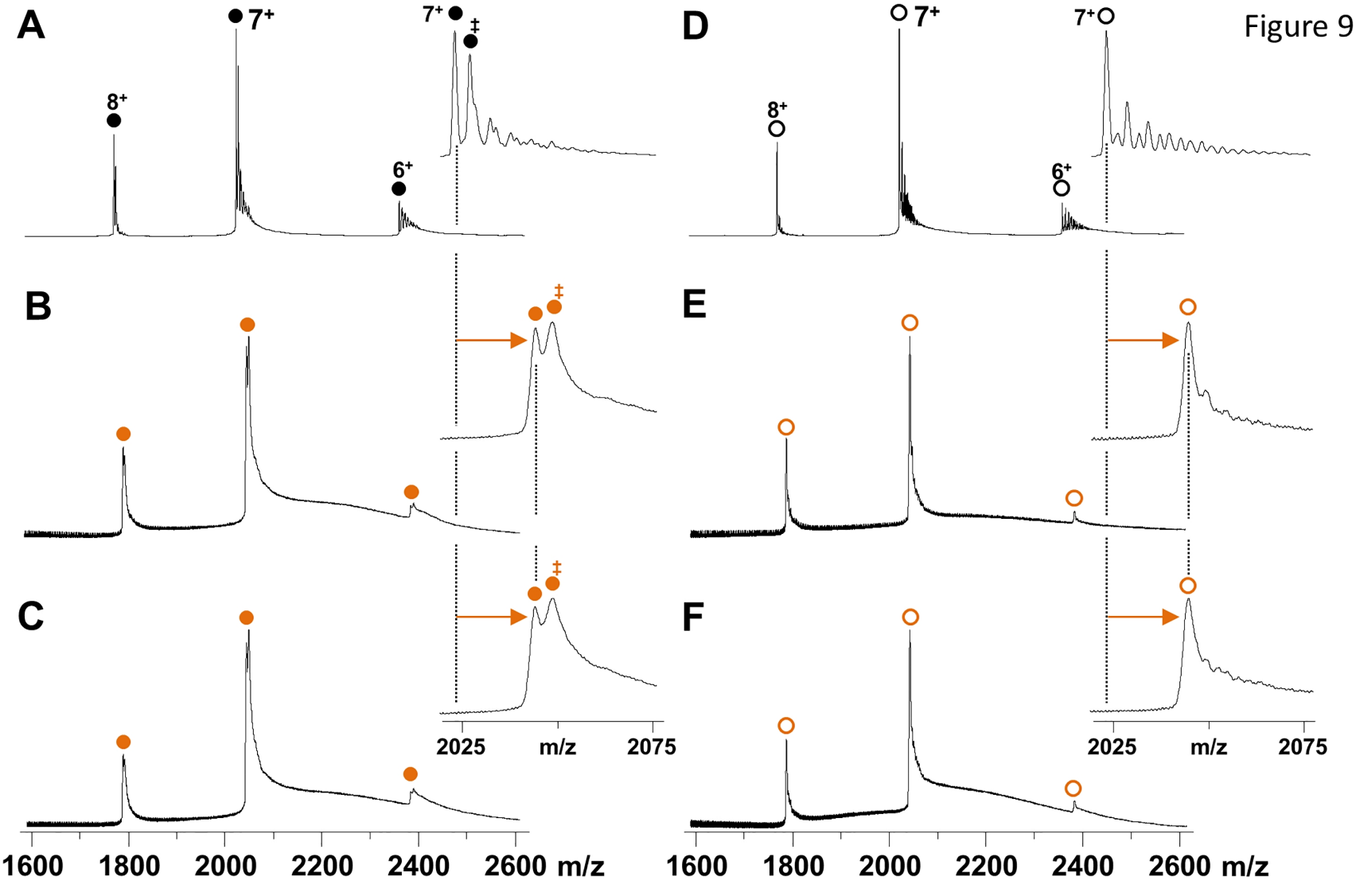

Figure 9

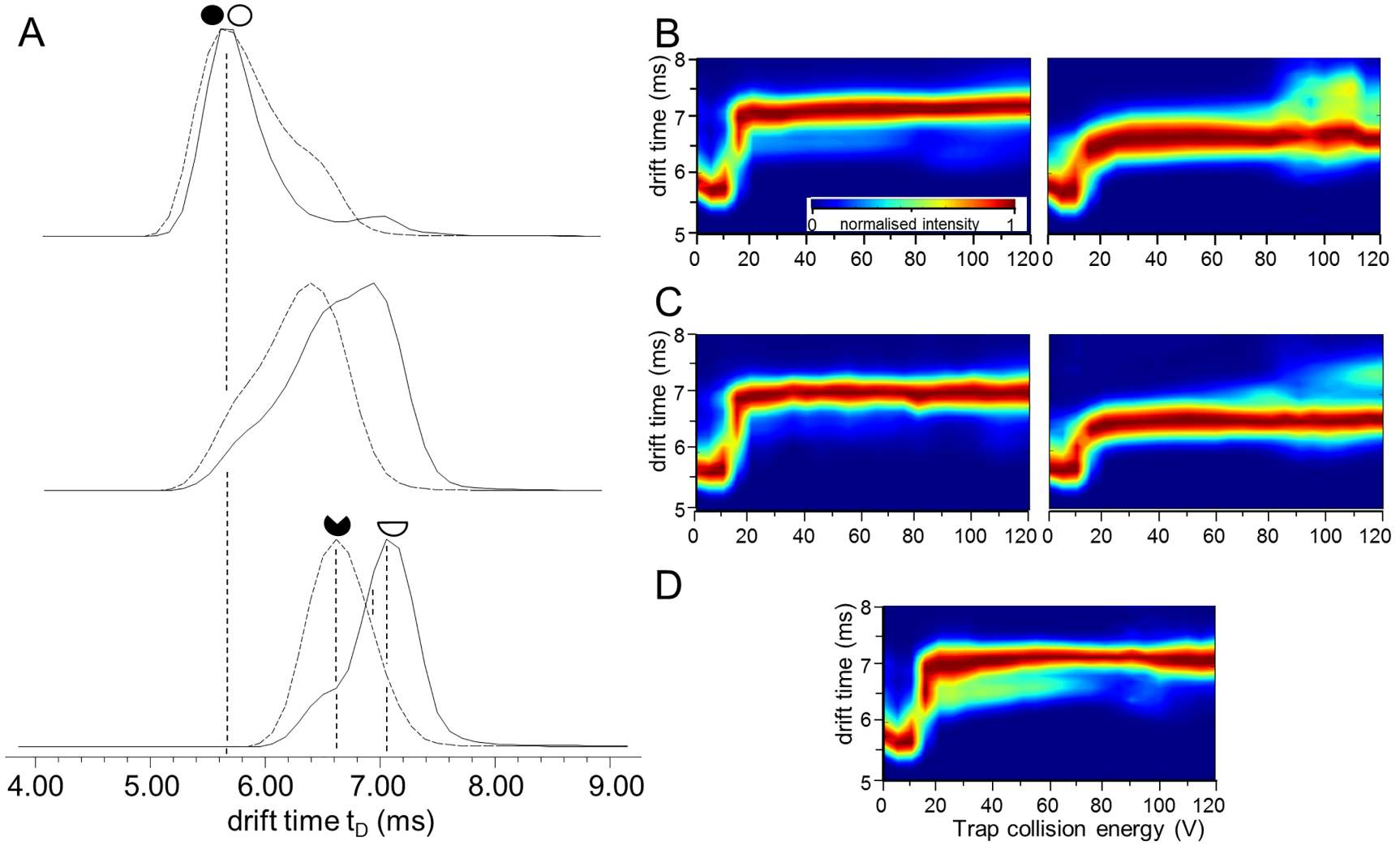
A
4.00
5.00
6.00
7.00
8.00
9.00
drift time t_D (ms)
B
drift time (ms)
8
7
6
5
0
normalised intensity
1
0
20
40
60
80
100
120
C
drift time (ms)
D
drift time (ms)
Trap collision energy (V)

Figure 10